ACCSCIENCE PUBLISHING

International Journal of Bioprinting

RESEARCH ARTICLE

# Three-dimensionally bioprinted skin-mimicking bilayer hydrogel dressing with compartmentalized antibacterial and pro-healing functions for diabetic wounds

**Wei Cao[1†], Danxi Li[2†], Qilong Yang[3†], Haiyang Qiu[1], Qinghua Guo[4], Shanshan Fu[1*], Jing Wang[1*], and Wei Lei[1*]**

[1]Department of Orthopedics, Xijing Hospital, The Fourth Military Medical University, Xi'an, Shaanxi, China

[2]Department of Thyroid, Breast and Vascular Surgery, Xijing Hospital, The Fourth Military Medical University, Xi'an, Shaanxi, China

[3]School of Public Health, Shaanxi University of Chinese Medicine, Xianyang, Shaanxi, China

[4]Department of Orthopaedics, The Fourth Medical Centre, Chinese PLA General Hospital, Beijing, China

(This article belongs to the *Special Issue: 3D Printing in Clinical Application*)

## Abstract

Diabetic wound healing remains a significant clinical challenge due to persistent infection and impaired tissue regeneration. This study presents a biomimetic, 3D-bioprinted bilayer hydrogel dressing with spatially compartmentalized functions to address these divergent requirements. The upper layer comprises chitosan hydrogel embedded with silver nanoparticles to provide rapid, broad-spectrum antibacterial activity against surface pathogens, and the lower layer consists of methacrylated silk fibroin hydrogel co-encapsulating epidermal stem cell-derived exosomes and metformin to create a pro-regenerative microenvironment in the deeper wound bed. Comprehensive *in vitro* characterization confirmed distinct physicochemical properties between the antibacterial upper layer and the porous, pro-healing lower layer. The upper layer exhibited synergistic bactericidal effects against *Staphylococcus aureus* and *Escherichia coli*, while the lower layer promoted M2 macrophage polarization, endothelial cell migration, and angiogenesis-related gene expression. In a diabetic mouse model of infected full-thickness wounds, compared to monolayer controls, the bilayer dressing significantly accelerated wound closure by increasing granulation tissue formation and neovascularization, while reducing bacterial burden. This compartmentalized design effectively integrates the complementary demands of infection control and tissue regeneration, offering a promising strategy for managing chronic diabetic ulcers.

***Keywords:*** 3D bioprinting; Diabetic wound; Hydrogel; Silver nanoparticles; Exosomes

†*These authors contributed equally to this work.*

***Corresponding authors:**
Shanshan Fu
(fufussss@163.com)
Jing Wang
(jingwang2014@163.com)
Wei Lei
(leiwei@fmmu.edu.cn)

**Citation:** Cao W, Li D, Yang Q, *et al.* Three-dimensionally bioprinted skin-mimicking bilayer hydrogel dressing with compartmentalized antibacterial and pro-healing functions for diabetic wounds. *Int J Bioprint.* 2026;12(3):026150134. doi: 10.36922/IJB026150134

**Received:** April 9, 2026

**Revised:** May 15, 2026

**Accepted:** May 18, 2026

**Published online:** May 19, 2026

## 1. Introduction

As the largest organ, the skin serves as a critical interface between the internal physiological environment and external pathogens, fulfilling essential functions including barrier defense, sensory transmission, thermoregulation, and metabolic homeostasis.[1] However, in diabetes mellitus, chronic hyperglycemia-induced inflammatory responses and microvascular complications render the skin exceptionally vulnerable, with approximately 15–34% of diabetic patients developing varying degrees of skin ulcers.[2,3] Without timely intervention, these ulcers frequently progress to deep tissue infections, sepsis, and even septic shock, potentially triggering multiple organ dysfunction syndrome and substantially increasing risks of amputation and mortality.[4,5] Nevertheless, the development of effective therapeutic strategies for diabetic wound healing remains a significant clinical challenge.

Currently, autologous or allogeneic skin transplantation represents the gold standard for repairing extensive skin defects.[6] However, the widespread clinical application of these approaches is severely constrained by donor site scarcity, immunological rejection, and pathogen transmission risks.[7,8] These limitations have catalyzed the emergence of tissue engineering and regenerative medicine approaches, particularly three-dimensional (3D) bioprinting technology, which enables the precise, layer-by-layer fabrication of living tissues with customizable architecture and controlled spatial distribution of cells and bioactive molecules. In recent years, natural polymers—specifically silk fibroin (SF) and chitosan (CS)—have garnered substantial attention as promising scaffold materials for skin tissue engineering. These biopolymers offer inherent advantages, including exceptional biocompatibility, biodegradability, and sustainability. SF, derived from *Bombyx mori* silkworm cocoons, exhibits tunable mechanical properties and remarkable cytocompatibility, making it particularly suitable for supporting tissue regeneration.[9,10] Meanwhile, CS, a deacetylated derivative of chitin, possesses intrinsic antibacterial properties and excellent hemostatic capacity.[11,12] However, the complex pathophysiology of diabetic wounds necessitates a multifunctional therapeutic approach that extends beyond passive scaffolding.

Local ischemia and exacerbated glycolytic metabolism in diabetic wounds induce oxidative stress and persistent inflammation, impairing the phenotypes and functions of macrophages and neutrophils, thereby creating favorable conditions for bacterial colonization.[13,14] Silver nanoparticles (AgNPs) exert broad-spectrum antibacterial activity through multiple mechanisms: (i) adsorption onto negatively charged bacterial membranes via electrostatic interactions; (ii) release of $Ag^+$ ions that bind respiratory enzymes to halt ATP synthesis; and (iii) generation of reactive oxygen species, causing oxidative damage to membranes and DNA. When incorporated into CS hydrogel, AgNPs demonstrate significant synergistic antibacterial efficacy.[15,16] However, the clinical utility of bare AgNPs is constrained by dose-dependent cytotoxicity to host tissues, arising from uncontrolled $Ag^+$ burst release.[17,18] Encapsulation within a hydrogel may address this limitation while enabling sustained $Ag^+$ release, maintaining moist wound environments, and providing bioadhesive properties essential for topical application in irregular diabetic wounds.

Meanwhile, effective diabetic wound repair requires robust regenerative signaling to overcome inherent repair deficiencies. Exosomes derived from epidermal stem cells (EpSCs-Exos) serve as potent paracrine mediators by delivering functional microRNAs (miRNAs) that orchestrate a regenerative microenvironment. These exosomes induce anti-inflammatory responses, angiogenesis, cell proliferation, and collagen synthesis through the activation of Notch, phosphoinositide 3-kinase/protein kinase B, transforming growth factor beta (TGF-β), and mitogen-activated protein kinase signaling pathways.[19-21] As a cell-free therapeutic strategy, EpSCs-Exos offer significant advantages over conventional stem cell treatments, including minimal immunogenicity, enhanced storage stability, and ease of preservation and transportation.[22,23] The encapsulation of these exosomes into a hydrogel could further amplify their therapeutic potential by enabling sustained release that maintains effective concentrations at the wound site, protecting exosomal cargoes from proteolytic degradation in the harsh diabetic microenvironment, and providing a biocompatible, moisture-retentive scaffold essential for cell migration and re-epithelialization.

Despite these individual advances, current single-layer dressings have yet to achieve clinical viability for simultaneously addressing the spatially and temporally divergent functional requirements of diabetic wound healing—namely, immediate infection control at the surface and sustained tissue regeneration in deeper layers. To bridge this gap, we hypothesized a biomimetic, compartmentalized approach (Figure 1). The upper layer utilizes CS hydrogel embedded with AgNPs to harness their antibacterial properties in diabetic wounds. Furthermore, CS exerts antibacterial effects via electrostatic membrane disruption, creating a multi-modal platform that prevents bacterial resistance through synergistic interactions with AgNPs.[24] The lower layer comprises methacrylated silk fibroin (SilMA) hydrogel co-encapsulating EpSCs-

Exos and metformin. This lower layer leverages SilMA's exceptional cytocompatibility, photocurable 3D printability, and sustained dual-release capability to create a pro-regenerative microenvironment.[25] Specifically, EpSCs-Exos drive cell infiltration, fibroblast recruitment, and angiogenesis, whereas metformin augments metabolic modulation, sustains angiogenic signaling, and potentiates the pro-regenerative functions of the exosomes, collectively maximizing tissue reconstruction in deeper wound strata.[26,27]

In this study, we developed a 3D bioprinted bilayer dressing based on this compartmentalized design and evaluated its therapeutic efficacy in a diabetic murine full-thickness infected wound model. This biomimetic construct simultaneously addresses infection prevention and tissue regeneration through spatially organized functionality, offering a promising clinically viable alternative to conventional skin grafting for the treatment of chronic diabetic wounds.

## 2. Materials and methods

### 2.1. Materials

Chitosan (degree of deacetylation ≥ 95%, molecular weight ~100–300 kDa), β-glycerophosphate disodium salt (β-GP; ≥98%), SilMA (degree of methacryloyl substitution ~30%), lithium phenyl-2,4,6-trimethylbenzoylphosphinate (LAP; photoinitiator, ≥95%), metformin hydrochloride (≥98%), and AgNPs (20 nm diameter) were purchased from Shanghai Dibo Chemicals Technology Co. (Shanghai, China). Dulbecco's Modified Eagle Medium/Nutrient Mixture F-12 (DMEM/F-12; Gibco, United States of America [USA]), high-glucose DMEM (25 mM glucose, Gibco, USA), fetal bovine serum (FBS; qualified, Gibco, USA), 0.25% and 0.05% trypsin-ethylenediaminetetraacetic acid (EDTA) (Gibco, USA), and phosphate-buffered saline (PBS; pH 7.4, Gibco, USA) were used for cell culture.

### 2.2. Preparation of epidermal stem cells from mice

#### *2.2.1. Epidermal stem cell isolation*

A total of six neonatal C57BL/6 mice were used in this study for primary epidermal stem cell isolation. The dorsal skin was harvested from these mice, and the epidermal cells obtained were pooled, expanded, and passage three cells were used for subsequent experiments. Briefly, the skin samples were rinsed three times with ice-cold PBS containing 1% penicillin/streptomycin to remove blood and debris. The cleaned skin was cut into small pieces and incubated in 0.25% trypsin-EDTA at 4 °C overnight. After digestion, the epidermis was gently peeled away from the dermis using fine forceps. The epidermal sheets were transferred to a fresh dish containing DMEM/F-12 supplemented with FBS to neutralize trypsin activity. Tissue was gently pipetted to release single cells, filtered through a 70 μm strainer (Corning, USA), and centrifuged at 300 ×*g* for 5 min. The pellet was resuspended in DMEM/F-12 medium. Cells were seeded onto collagen IV-coated dishes (10 μg/mL, overnight at 4 °C) and cultured at 37 °C/5% $CO_2$. Non-adherent cells were removed after two days by medium change, with subsequent renewal every two days. At 80–90% confluence, cells were passaged using 0.05% trypsin-EDTA, and passage three cells were used for subsequent experiments.

#### *2.2.2. Epidermal stem cell characterization*

Total protein was extracted using RIPA lysis buffer supplemented with phenylmethylsulfonyl fluoride, and concentrations were determined using the bicinchoninic acid (BCA) assay (Thermo Fisher, United States of America [USA]). Equal amounts of protein were separated by sodium dodecyl sulfate–polyacrylamide gel electrophoresis and transferred onto polyvinylidene fluoride membranes (Thermo Fisher, USA). After blocking with 5% skim milk in Tris-buffered saline (TBS) with Tween 20, membranes were incubated overnight at 4 °C with primary antibodies against integrin-α6 (1:500; 27189-1-AP, Proteintech, USA) and Krt15 (1:500; 60247-1-Ig, Proteintech, USA), and GAPDH (1:1000; loading control; 10494-1-AP, Proteintech, USA). Following incubation with horseradish peroxidase (HRP)-conjugated secondary antibodies (1:5000; RGAR001, Proteintech, USA) for 1 h at room temperature, immunoreactive bands were visualized using an enhanced chemiluminescence detection kit and quantified with ImageJ software (version 2.1.0, NIH, USA).

### 2.3. Isolation and characterization of epidermal stem cell-derived exosomes

#### *2.3.1. Epidermal stem cell-derived exosome isolation*

Cell culture supernatant was collected, and EpSCs-Exos were isolated by differential centrifugation. Briefly, the supernatant was centrifuged sequentially at 300 ×*g* for 10 min, 2,000 ×*g* for 10 min, 10,000 ×*g* for 30 min, and finally at 100,000 ×*g* for 70 min at 4 °C. The resulting pellets were resuspended in PBS, centrifuged again at 100,000 ×*g* for 70 min, and finally resuspended in 100 μL of PBS. The exosome suspension was filtered through a 0.22 μm filter, and protein content was measured using an enhanced BCA assay kit. Purified EpSCs-Exos were stored at −80 °C until further use.

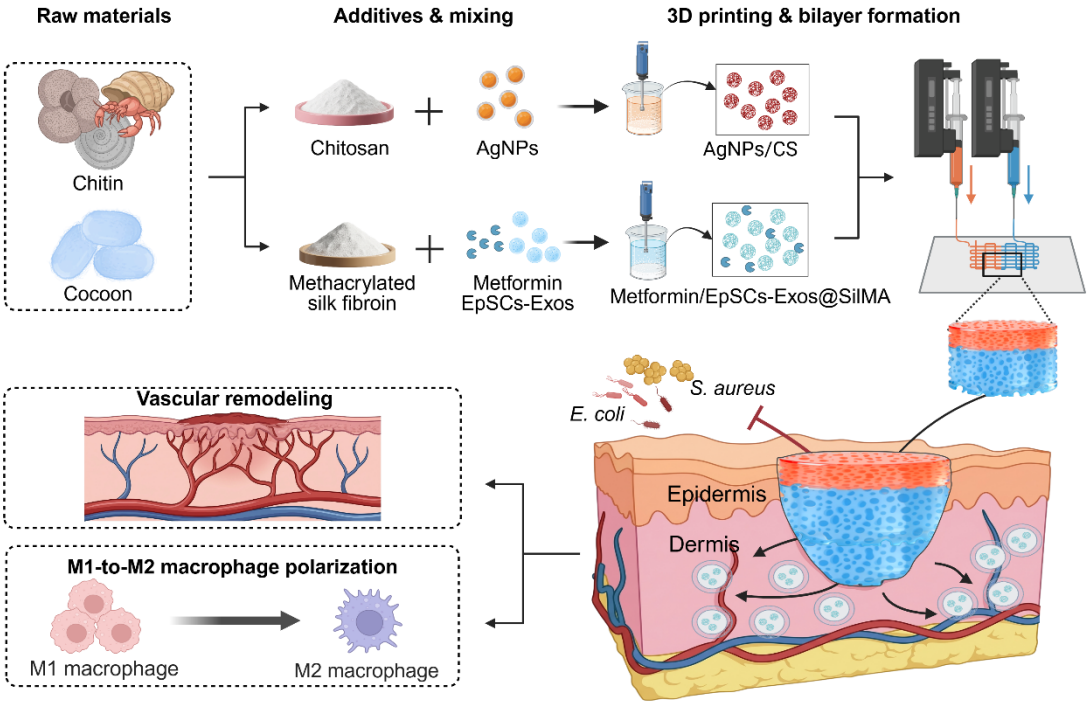


**Figure 1.** Schematic illustration of the preparation and compartmentalized therapeutic mechanisms of the 3D-bioprinted skin-mimicking bilayer hydrogel dressing. Created in BioRender. Feng, Y. (2026) https://BioRender.com/22s4dkj

#### *2.3.2. Epidermal stem cell-derived exosomes characterization*

Exosome morphology was examined using transmission electron microscopy (TEM; HT7800, Hitachi, Japan). For TEM analysis, 15 μL of the exosome sample was placed onto a copper grid and left to stand for 1 min. The grid was handled carefully with forceps to avoid damage. After blotting the grid dry with filter paper, the sample was stained for 1 min at room temperature with 15 μL of uranyl acetate. Following staining, the grid was blotted dry again and placed under a lamp for 10 min before observation and imaging. Particle concentration and size distribution were determined by nanoparticle tracking analysis (NTA; Nanosight NS300, Malvern, United Kingdom). Briefly, 1 mL of the exosome suspension was drawn into a syringe. Western blotting (WB) was performed to detect the exosomal markers TSG101 and Alix (all from Protein Tech, China). To assess the structural integrity of exosomes after release from the MetEx–Sil hydrogel, exosomes collected from the day-3 release medium were negatively stained and examined by TEM using the protocol described above.

### 2.4. Preparation of printable hydrogel bioinks

#### *2.4.1. Preparation of thermosensitive chitosan-based bioink for the upper layer*

Chitosan was dissolved in 1.0% (v/v) acetic acid solution at a concentration of 3% (w/v) under magnetic stirring at room temperature overnight until a homogeneous transparent solution was obtained. Subsequently, pre-cooled β-GP solution was added dropwise under ice-bath conditions to achieve a final concentration of 8% (w/v), imparting thermosensitive sol–gel transition properties to the ink. To enhance printability and structural fidelity, gelatin was supplemented at 2% (w/v) and stirred at 25–30 °C until complete dissolution. An AgNP dispersion was then incorporated at a final concentration of 0.1 mg/mL under light-protected conditions, followed by stirring for 20 min to ensure uniform physical distribution without chemical grafting or carrier encapsulation. This physical incorporation is facilitated by the abundant amino ($-NH_2$) and hydroxyl (–OH) groups present on the CS backbone, which stabilize AgNPs via electrostatic attraction and hydrogen bonding, thereby ensuring homogeneous

dispersion throughout the hydrogel network. The resulting solution was degassed at 4 °C for 30 min to eliminate bubbles prior to printing.

#### *2.4.2. Preparation of photocurable SilMA bioink for the lower layer*

SilMA solution was prepared at 10% (w/v) concentration, and photoinitiator LAP was added at 0.25% (w/v) under light-protected stirring until fully dissolved. Metformin hydrochloride was physically incorporated at 2 mg/mL and stirred at room temperature for 15–20 min. Subsequently, EpSCs-Exos were gently added at a final concentration of 1.0–1.5 × $10^9$ particles/mL (protein equivalent 300 μg/mL) under dark conditions. The mixture was gently agitated for 5–10 min to achieve uniform dispersion via non-covalent interactions (hydrogen bonding, hydrophobic interactions, and electrostatic adsorption), avoiding vigorous vortexing or sonication to preserve exosomal membrane integrity. The system was vacuum-degassed and transferred to light-protected syringes for immediate use. The photocrosslinking mechanism relies on free-radical polymerization of the methacrylate moieties grafted onto SF upon subsequent exposure to 405 nm light in the presence of LAP, generating a robust covalently crosslinked SilMA network. Within this three-dimensional mesh, EpSCs-Exos and metformin are physically entrapped via non-covalent interactions (hydrogen bonding, hydrophobic interactions, and electrostatic adsorption), which maintain the structural integrity and bioactivity of the exosomal membranes while enabling their sustained release from the scaffold.

### 2.5. 3D bioprinting of asymmetric bilayer dressing

The bilayer hydrogel was fabricated via extrusion-based 3D bioprinting employing sequential crosslinking strategies. For the lower layer, the metformin/EpSCs-Exos@SilMA (MetEx–Sil) bioink was loaded into a sterile syringe fitted with a 20 G nozzle (inner diameter 0.6 mm) and deposited onto a sterile substrate in a regular grid pattern (30 mm × 30 mm) with 0/90° alternating orientation. The printing parameters were set as line spacing 0.8 mm, printing speed 6–8 mm/s, and pneumatic pressure 80–120 kPa. Immediately after deposition, the layer was subjected to 405 nm light irradiation at 30 mW/$cm^2$ for 30–60 s to induce in situ photocrosslinking of SilMA, forming a stable three-dimensional network that physically encapsulated the exosomes and metformin.

For the upper layer, the AgNPs/CS (Ag–CS) bioink was loaded into a separate syringe with a 22 G nozzle (inner diameter 0.41 mm) and directly deposited onto the surface of the solidified lower layer with matching dimensions and thickness. To achieve a dense barrier structure, the line spacing was reduced to 0.4–0.5 mm, and the printing speed decreased to 4–6 mm/s. Following completion of upper layer deposition, the construct was incubated at 37 °C for 20–30 min to promote thermogelation of the CS/β-GP system, resulting in a stable bilayer dressing with total dimensions of 30 mm × 30 mm × 4 mm. The upper layer exhibited a dense pore structure due to reduced line spacing and higher polymer concentration, while the lower layer displayed loose, interconnected pores attributed to larger line spacing and moderate solid content.

### 2.6. Bilayer hydrogel dressing characterization

#### *2.6.1. Fourier transform infrared spectroscopy*

Chemical composition was analyzed using a Fourier transform infrared (FTIR) spectrometer (Nicolet iS50, USA). Lyophilized samples of the upper layer (Ag–CS), lower layer (MetEx–Sil), and bilayer dressing were ground with potassium bromide (1:100, w/w) and pressed into discs. Spectra were recorded at 400–4,000 $cm^{-1}$ (resolution 4 $cm^{-1}$, 32 scans). Characteristic peaks were identified: CS (-OH/-NH at ~3,300 $cm^{-1}$, amino at ~1,600 $cm^{-1}$), SF (amide I/II at ~1,620/1,500 $cm^{-1}$), confirming physical composite formation without new covalent bonds.

#### *2.6.2. Surface wettability assessment*

Contact angles were measured using the sessile drop method (goniometer OCA 25, Germany). A 5 μL water droplet was deposited onto the upper layer, lower layer, and bilayer dressing surfaces at 25 °C. Images were captured within 10 s and analyzed using Laplace-Young fitting. Results represent mean ± standard deviation ($n$ = 3).

#### *2.6.3. Swelling behavior analysis*

Pre-weighed dry samples were immersed in PBS (pH 7.4) at 37 °C. Weights were recorded at 0.5, 1, 2, 4, 8, 12, 24, and 48 h.

$$\text{Swelling ratio (\%)} = [(W_2 - W_1)/W_1] \times 100\% \quad (1)$$

where $W_1$ and $W_2$ represent initial and swollen weights, respectively.

#### *2.6.4. Rheological characterization*

Viscoelastic properties were measured using a rotational rheometer (MCR 302, Austria) with 20 mm parallel plates at 37 °C. Frequency sweeps (0.1–100 rad/s, 1% strain within linear viscoelastic region) were performed on cylindrical samples (diameter 20 mm, thickness 2 mm for single layers; 4 mm for bilayer). Storage modulus (G') and loss modulus (G") were recorded ($n$ = 3).

#### 2.6.5. Mechanical testing

The mechanical properties of the hydrogels were evaluated by tensile and compression experiments via a universal material testing machine (Instron 5943, USA) equipped with a 500 N load cell. For the tensile experiments, rectangular samples (30 mm in length, 10 mm in width, and 2 mm in thickness) were stretched at a rate of 10 mm/min. The tensile modulus was calculated from the linear region (10–30% strain) of the stress–strain curve. For the compression experiments, cylindrical samples (10 mm in diameter and 5 mm in height) were compressed at a rate of 2 mm/min with a strain range of 0–70%. The compression modulus was determined from the slope of the stress–strain curve in the 10–30% strain region. All tests were conducted at room temperature ($n$ = 3 per group).

#### 2.6.6. Scanning electron microscopy

Microstructural morphology was examined using scanning electron microscopy (SEM; Hitachi SU8010, Japan). Samples were freeze-dried, fractured to expose cross-sections, and sputter-coated with gold-palladium (10 nm). For the bilayer dressing, specific emphasis was placed on the interfacial region; samples were fractured perpendicular to the layer plane to visualize the junction zone and transition from the dense upper layer (Ag–CS) to the porous lower layer (MetEx–Sil). Imaging was performed at 5–10 kV (100–5,000×). Pore size was analyzed using ImageJ ($n$ = 3).

#### 2.6.7. In vitro $Ag^+$ ion release test

Cylindrical Ag–CS hydrogels (ø = 10 mm, h = 5 mm) were immersed in 2 mL PBS (pH 7.4, 37 °C) under orbital shaking (100 rpm). Following a sequential sampling protocol, 200 μL aliquots were withdrawn at 24-h intervals for 7 days and replaced with fresh PBS to maintain sink conditions. Silver concentration was quantified by inductively coupled plasma mass spectrometry (NexION 2000, PerkinElmer, USA).

#### 2.6.8. In vitro metformin release test

Hydrogel specimens were incubated in 1 mL PBS (37 °C) with gentle agitation. At each time point (0–7 days, 24-hour intervals), 500 μL release medium was collected and replenished with fresh PBS. Metformin concentration was determined by UV–Vis spectrophotometry (λmax = 233 nm; NanoDrop 2000, Thermo Fisher Scientific, USA) against a linear calibration curve.

#### 2.6.9. Fluorescent visualization and quantification of exosome release

EpSCs-Exos were pre-stained with 1,1'-dioctadecyl-3,3,3',3'-tetramethylindocarbocyanine perchlorate (DiI) prior to incorporation. MetEx–Sil constructs were bathed in PBS (37 °C). Spatiotemporal distribution was assessed by confocal laser scanning microscopy at 1, 3, 7, and 14 days to reconstruct 3D fluorescence profiles. Cumulative exosome release was quantified by BCA protein assay at 24-h intervals over 7 days.

### 2.7. Biocompatibility evaluation

#### 2.7.1. Live/dead staining

To assess the biocompatibility of the material extracts, human skin fibroblasts (PCS-201-012, ATCC, USA) were seeded on 12-well plates and exposed for 1 and 3 days to extracts from four groups: Control (fresh culture medium without any material extract), Ag–CS, MetEx–Sil, and Ag–CS/MetEx–Sil. The medium was then removed, and cells were washed twice with PBS and stained with calcein-AM/propidium iodide (PI) (Beyotime, China) for 30 min at 37 °C. Stained cells were examined under a fluorescence microscope to visualize live and dead cells. To extend the biocompatibility assessment to an additional wound-relevant cell type, human umbilical vein endothelial cells (HUVECs; CRL-1730, ATCC, USA) were cultured under identical extract exposure conditions and subjected to the same live/dead staining protocol.

#### 2.7.2. CCK8 assay

Human skin fibroblasts grown in 96-well plates were treated with the material extracts from each of the four groups for 1, 3, and 5 days. CCK-8 solution (Beyotime, China) was added to each well. After 0.5 h of incubation, absorbance at 450 nm was measured using a microplate reader (TECAN Spark, Switzerland). The resulting absorbance values were used to evaluate cell proliferation as an additional indicator of biocompatibility.

#### 2.7.3. Hemolysis assay

Blood was collected from one mouse in each independent experiment, and five independent experiments were performed to generate five biological replicates per group ($n$ = 5). Fresh blood was collected from 4-week-old C57BL/6 mice into sodium citrate anticoagulant tubes (1:9, v/v), centrifuged at 2,000 rpm for 10 min to isolate red blood cells (RBCs), and washed three times with TBS (pH 7.2). The RBCs were resuspended in TBS to prepare a 2.5% (v/v) suspension. Ag–CS, MetEx–Sil, and Ag–CS/MetEx–Sil hydrogel samples were separately incubated with 1.0 mL of the RBC suspension at 37 °C for 1 h, using PBS and $H_2O$ as negative and positive controls, respectively. After centrifugation at 2,000 rpm for 5 min, the supernatant was collected, and the optical density was measured at 450 nm using a microplate reader. The hemolysis percentage was

calculated using the following equation:

$$\text{Hemolysis ratio}(\%) = \frac{(OD_{sample} - OD_{negative})}{(OD_{positive} - OD_{negative})} \times 100\% \quad (2)$$

with hemolysis rates below 5% considered acceptable according to ISO 10993-4 standards ($n$ = 5 per group).

### 2.8. Antibacterial evaluation

#### *2.8.1. Bacterial culture and material extract preparation*

*Escherichia coli* (ATCC 25922) and *Staphylococcus aureus* (ATCC 25923) were used as the test strains. Bacteria were grown overnight in Luria–Bertani (LB) broth at 37 °C with shaking. The bacterial suspension was then diluted with fresh LB broth to an optical density of approximately 0.5 at 600 nm (OD600 ≈ 0.5), corresponding to about $1 \times 10^8$ colony-forming units (CFUs)/mL. Material extracts were prepared for three groups: Control (LB broth without any material extract), CS, and Ag–CS.

#### *2.8.2. Bacterial live/dead staining*

To evaluate the antibacterial effect of material extracts, 100 μL of each bacterial suspension (approximately $1 \times 10^8$ CFU/mL) was mixed with 900 μL of material extract from each group and incubated at 37 °C for 4 h. After incubation, the mixtures were centrifuged at 5,000 ×$g$ for 5 min, and the pellets were washed twice with sterile PBS. The bacteria were then stained with a Live/Dead BacLight Bacterial Viability Kit (Thermo Fisher, USA) containing SYTO 9 and PI. Staining was performed at room temperature in the dark for 30 min. Stained bacterial samples were placed onto glass slides and observed under a fluorescence microscope. Live bacteria with intact membranes appeared green, while membrane-compromised dead bacteria appeared red. Images were captured from randomly selected fields for each group.

#### *2.8.3. Bacterial colony counting assay*

For quantitative assessment of antibacterial activity, 100 μL of each bacterial suspension (approximately $1 \times 10^8$ CFU/mL) was mixed with 900 μL of material extract from the Control, CS, or Ag–CS groups and incubated at 37 °C for 4 h. After incubation, the mixtures were serially diluted 10-fold with sterile PBS. From each dilution, 100 μL was spread onto LB agar plates in triplicate. The plates were incubated at 37 °C for 16 h. Colonies on each plate were counted, and the number of viable bacteria (CFU/mL) was calculated.

### 2.9. Immunomodulation evaluation

#### *2.9.1. Immunofluorescence staining*

To mimic the diabetic wound microenvironment, RAW264.7 macrophages (TIB-71, ATCC, USA) were cultured in high-glucose, high-fat (HGHF) medium containing high-glucose DMEM (25 mM glucose) supplemented with 200 μM palmitic acid, 10% FBS, and 1% penicillin/streptomycin. Material extracts were prepared by immersing Met–Sil (SilMA hydrogels incorporated with metformin only) and MetEx–Sil (SilMA hydrogels incorporated with metformin and EpSCs-Exos) specimens in HGHF medium at a ratio of 0.2 g/mL (or 1.25 $cm^2$/mL) for 72 h at 37 °C, followed by filtration through 0.22 μm syringe filters. Cells were divided into three groups ($n$ = 6)—Control (pure HGHF medium), Met–Sil, and MetEx–Sil (HGHF medium supplemented with 25% v/v respective extracts)—and incubated for 2 days. Immunofluorescence (IF) staining was subsequently performed to evaluate macrophage polarization. Briefly, cells were fixed with 4% paraformaldehyde for 30 min, permeabilized with 0.1% Triton X-100 for 10 min, and blocked with 3% bovine serum albumin (BSA; Thermo Fisher Scientific, USA) for 30 min at room temperature. After incubation with primary antibodies CD86 (M1 marker; 1:500; 83213-1-RR, Proteintech, USA) or Arg-1 (M2 marker; 1:500; 53-3697-82, Thermo Fisher Scientific, USA) overnight at 4 °C and thorough washing with PBS, secondary antibodies were applied for 2 h at room temperature, followed by nuclear counterstaining with DAPI. Fluorescence images were captured under standardized microscopy settings to ensure consistency across all experimental groups.

#### *2.9.2. Flow cytometric analysis*

Following treatment with respective extracts under HGHF conditions as described above, cells were harvested at days 2 and 7, washed twice with cold PBS containing 1% BSA, and resuspended at $1 \times 10^6$ cells/mL. After Fc receptor blocking (anti-mouse CD16/CD32; 15 min, 4 °C; 565502, BD Biosciences, USA), cells were stained with fluorochrome-conjugated antibodies against CD86-FITC (M1 marker; 1:100; FITC-98025, BioLegend, USA) or CD206-PE (M2 marker; 1:100; PE-98031, BioLegend, USA) for 30 min at 4 °C in the dark. Following two PBS washes, cells were resuspended in 500 μL PBS and analyzed using a BD FACSCalibur flow cytometer (BD Biosciences, USA). For each sample, 10,000 events were acquired and analyzed using FlowJo software (v10.0, Tree Star, USA) to quantify the percentages of $CD86^+$ (M1) and $CD206^+$ (M2) macrophages.

### 2.10. Pro-angiogenic evaluation

#### *2.10.1. Scratch wound healing assay*

Human umbilical vein endothelial cells were treated under the same HGHF and material-extract exposure conditions as RAW264.7 macrophages. For wound healing assessment, confluent monolayers in 6-well plates were scratched with a sterile 200 μL pipette tip, washed thrice with PBS, and incubated in serum-free DMEM/F12 supplemented with respective material extracts (Control, Met–Sil, or MetEx–Sil). Phase-contrast images were captured at 0, 24, and 48 h (Nikon Eclipse TS2, Japan), and migration rates were determined using ImageJ by normalizing residual wound area to initial values.

#### *2.10.2. Transwell migration assay*

Human umbilical vein endothelial cell migration was assessed using 24-well Transwell chambers (8.0 μm pore size; Merck, Germany). Cells were seeded at $5 \times 10^4$ cells/well in 200 μL serum-free DMEM/F12 into the upper chamber. The lower chamber contained 600 μL of the corresponding material extract (Control, Met–Sil, or MetEx–Sil) diluted in complete medium. After 24 h incubation at 37 °C with 5% $CO_2$, non-migrated cells on the upper membrane surface were gently removed using a cotton swab. Migrated cells on the lower surface were fixed with 4% paraformaldehyde (15 min), stained with 0.1% crystal violet in methanol (20 min), and rinsed with PBS. Cells were counted in five random fields per well at 40× magnification under an inverted light microscope (Nikon Eclipse TS2, Nikon, Japan).

### 2.11. RNA sequencing and bioinformatics analysis

Following the aforementioned culture protocol, HUVECs were assigned to two groups ($n = 3$ per group): the Control group (cultured in HGHF medium alone), and the MetEx–Sil group (cultured in HGHF medium supplemented with 25% v/v corresponding MetEx–Sil hydrogel dressing extract). After 72 h incubation, total RNA was extracted using TRIzol reagent (Invitrogen, USA) and subjected to paired-end sequencing (PE150) on an Illumina NovaSeq 6000 platform (Illumina, USA). Differentially expressed genes (DEGs) were identified using DESeq2 ($|\log_2(\text{fold change})| > 1$, FDR < 0.05). Gene Ontology (GO) enrichment analysis was conducted using clusterProfiler to identify significantly enriched biological processes. Gene Set Enrichment Analysis (GSEA) was performed using MSigDB to determine the enrichment of predefined gene sets. Furthermore, protein–protein interaction (PPI) network analysis was constructed using the STRING database to explore the interactions among DEGs.

### 2.12. Infected diabetic wound model treatment

#### *2.12.1. Diabetic model establishment*

All animal procedures were approved by the Institutional Animal Care and Use Committee of the Air Force Medical University (Approval No. IACUC-20240561). A total of 48 male C57BL/6J mice (6–8 weeks old, 20–22 g) were purchased from the Experimental Animal Center of the Air Force Medical University and housed under standard conditions (22 ± 2 °C, 50–60% humidity, 12 h light/dark cycle) with free access to food and water. Type 2 diabetes mellitus (T2DM) was induced by feeding a high-fat diet (HFD; 60% kcal from fat) beginning at four weeks before surgery (−4W). After two weeks of HFD feeding, streptozotocin (20 mg/kg/day for five consecutive days; Aladdin, China) dissolved in citrate buffer (0.1 M, pH 4.5) was administered intraperitoneally after overnight fasting at −2W. The HFD was maintained continuously until the surgical intervention at 0D. Blood glucose levels were monitored via tail-tip sampling. Mice with non-fasting blood glucose consistently exceeding 16.7 mmol/L were considered diabetic and included in subsequent experiments.

#### *2.12.2. Wound creation and treatment protocol*

Eight weeks after diabetes induction, full-thickness excisional wounds were created on the dorsal skin of the mice. Briefly, mice were anesthetized using isoflurane inhalation (2–3% in oxygen), and the dorsal hair was shaved and sterilized with 75% ethanol. An 8-mm-diameter full-thickness skin defect was created using a sterile biopsy punch. Mice were randomly divided into four groups ($n = 6$ per group): (i) Control group treated with commercial sterile gauze; (ii) Ag–CS monolayer group; (iii) MetEx–Sil monolayer group; and (iv) Ag–CS/MetEx–Sil bilayer group. Wounds were inoculated with S. aureus ($10^6$ CFU/100 μL) suspension immediately after wounding. At 24 h post-infection, the respective hydrogel formulations were topically applied to the wound.

#### *2.12.3. Wound monitoring and bacterial assessment*

Wounds were photographed at 0, 5, 10, and 15 days post-treatment using a digital camera with a standardized ruler placed adjacent to the wound. The wound area was quantified using ImageJ software by tracing the wound margins. The remaining wound area (%) was calculated as follows:

$$\text{Remaining wound area } (\%) = \frac{\text{Residual wound area}}{\text{Initial wound area}} \times 100\% \quad (3)$$

To evaluate antibacterial efficacy *in vivo*, wound tissues were

harvested on day 5 post-treatment. Briefly, wound tissues were excised, homogenized in 1 mL sterile PBS, and serially diluted. Aliquots (50 μL) of the diluted homogenates were spread onto LB agar plates and incubated at 37 °C for 18 h.

#### *2.12.4. Histological and immunohistochemical analysis*

On days 10 and 15 post-treatment, mice were euthanized, and wound tissues were harvested, fixed in 10% neutral-buffered formalin for 48 h, and embedded in paraffin. Serial sections (5 μm thick) were prepared for histological and immunohistochemical staining. For histological evaluation, sections were stained with hematoxylin and eosin (H & E) to assess granulation tissue formation, and Masson's trichrome staining was performed to evaluate collagen deposition and extracellular matrix remodeling. Granulation tissue thickness was measured at the thickest point of the wound bed using ImageJ software. For immunohistochemistry, sections were deparaffinized, rehydrated, and subjected to antigen retrieval using citrate buffer (pH 6.0) in a pressure cooker. Endogenous peroxidase activity was blocked with 3% hydrogen peroxide, and non-specific binding was blocked with 10% goat serum. Sections were incubated overnight at 4 °C with primary antibodies against CD86 (M1 macrophage marker; 1:500; 83213-1-RR, Proteintech, USA), CD163 (M2 macrophage marker; 1:500; 83285-4-RR, Proteintech, USA), and CD31 (endothelial cell marker; 1:500; 28083-1-AP, Proteintech, USA). After washing, sections were incubated with HRP-conjugated secondary antibodies for 2 h at room temperature. Diaminobenzidine was used as the chromogen, and sections were counterstained with hematoxylin. Positive staining areas were quantified using ImageJ software.

#### *2.12.5. Systemic biosafety assessment*

At day 15, immediately following euthanasia and wound tissue harvest, major organs, including the heart, liver, spleen, lungs, and kidneys, were excised, rinsed with sterile PBS, fixed in 10% neutral-buffered formalin for 48 h, and embedded in paraffin. Serial sections (5 μm) were prepared and stained with H & E to assess potential pathological changes, including inflammatory cell infiltration, tissue necrosis, hemorrhage, or structural damage. Slides were examined under a light microscope by a pathologist blinded to the experimental groups.

### 2.13. Statistical analysis

Quantitative data were presented as mean ± standard deviation. Differences between the two groups were evaluated using two-tailed Student's *t*-tests. For comparisons involving multiple groups, one-way or two-way ANOVA was conducted where appropriate. All statistical analyses were carried out using GraphPad Prism 9 (GraphPad, USA), with a significance threshold set at $p < 0.05$. The significance levels are denoted by asterisks as follows: ns, not significant ($p > 0.05$); * for $p < 0.05$; ** for $p < 0.01$; *** for $p < 0.001$.

## 3. Results

### 3.1. Isolation and characterization of epidermal stem cell-derived exosomes

As depicted in Figure 2A, the primary EpSCs were successfully isolated from mouse skin tissues, displaying high proliferative capacity and forming colonies (Figure 2B). WB analysis confirmed that EpSCs were positive for the epithelial stem cell markers Integrin-α6 and Krt15 (Figure 2C). EpSCs-Exos were subsequently harvested from conditioned media via successive ultracentrifugation and subjected to comprehensive physicochemical and biochemical characterization.

Cryo-TEM revealed spherical vesicles enclosed by a characteristic phospholipid bilayer membrane, consistent with canonical exosomal ultrastructure (Figure 2D). NTA further quantified the size distribution profile, indicating a predominant population with a mean hydrodynamic diameter of 133.2 nm (Figure 2E). The yield was determined as $2.1 \times 10^{11}$ particles per milliliter of culture medium. In addition, immunoblotting was performed to confirm the presence of typical EpSCs-Exos markers Alix and TSG101 (Figure 2F). Collectively, these analytical data substantiate the high purity and functional integrity of the isolated EpSCs-Exos, validating their suitability for downstream functional investigations.

### 3.2. Preparation and characterization of the Ag–CS/MetEx–Sil hydrogel

#### *3.2.1. Morphology*

The morphology of the bilayer hydrogel is depicted in Figure 3A–3F, showing differences in porous architecture between the upper and lower layers. The upper Ag–CS layer displayed a relatively dense and continuous network characterized by thickened pore walls, with an average pore size of 10.49 ± 3.15 μm (Figure 3A and 3D). In contrast, the lower MetEx–Sil layer demonstrated markedly distinct microscopic morphology, featuring larger pores and a loose three-dimensional porous network, with an average pore size of 13.93 ± 4.00 μm (Figure 3C and 3F). Cross-sectional views clearly revealed a distinct interfacial boundary between the upper dense layer and the lower porous layer (Figure 3E). Although a structural transition zone was visible at the interface, no obvious cracks,

delamination, or fractured gaps were observed, suggesting that appropriate integration between the upper and lower layers was achieved during the layer-by-layer printing and in situ curing process.

#### 3.2.2. Fourier transform infrared spectral analysis

The FTIR spectra revealed characteristic absorption features corresponding to the respective compositions of the upper Ag–CS layer, the lower MetEx–Sil layer, and the bilayer construct (Figure 3G). The upper Ag–CS layer exhibited a broad band at ~3,300 $cm^{-1}$ (O–H/N–H stretching) and peaks at ~1,600 $cm^{-1}$ (N–H bending of amino groups) and 1,000–1,100 $cm^{-1}$ (C–O–C glycosidic vibrations), consistent with CS structure. For the lower MetEx–Sil layer, a broad peak at ~3,300 $cm^{-1}$ was similarly observed, alongside prominent characteristic amide bands at approximately 1,620 $cm^{-1}$, consistent with the molecular structure of SilMA. Additionally, subtle alterations in the fingerprint region (<1,500 $cm^{-1}$) and C–H stretching region (~2,800–3,000 $cm^{-1}$) indicated molecular interactions between metformin, EpSCs-Exos, and the SilMA matrix, suggesting successful incorporation. The bilayer spectrum retained principal peaks of both individual layers without significant peak shifts, confirming successful construction and maintaining chemical integrity after compositing. No emergence of new strong characteristic peaks in the bilayer construct indicated that the system was primarily formed through physical combination rather than covalent bonding.

#### 3.2.3. Hydrophilicity

Contact angle measurements indicated variations in surface wettability among the three groups (Figure 3H). The Ag–CS layer exhibited the highest contact angle, suggesting a relatively compact surface structure with limited droplet spreading capacity. In contrast, the MetEx–Sil layer displayed the lowest contact angle, demonstrating enhanced hydrophilicity consistent with its porous network architecture and superior water absorption capacity.

#### 3.2.4. Rheological characterization

Frequency sweep results demonstrated that the storage modulus (G') exceeded the loss modulus (G") across the entire frequency range for all groups, confirming dominant elastic responses, stable three-dimensional network structures, and favorable gelation properties (Figure 3I and 3J). Both G' and G" exhibited gradual increases with rising angular frequency, indicating frequency-dependent behavior under dynamic perturbation while maintaining gel-dominated characteristics. Quantitatively, G' followed the trend: Ag–CS layer > Ag–CS/MetEx–Sil bilayer hydrogel > MetEx–Sil layer, with G" following a similar trend. The upper layer exhibited the highest G', suggesting greater crosslinking density and deformation resistance. The lower layer presented the lowest G', suggesting a softer network with reduced mechanical constraints. The bilayer construct displayed intermediate G' values, preserving the flexibility of the lower layer while gaining enhanced mechanical stability from the upper dense structure. Correspondingly, G" values were highest in the Ag–CS layer and lowest in the MetEx–Sil layer, with the bilayer construct at intermediate levels.

#### 3.2.5. Mechanical characterization

To further verify the structural integrity of the bilayer dressing under physical stress, quantitative tensile and compression testing were performed (Figure S1). As shown in Figure S1, the Ag–CS upper layer displayed the highest tensile modulus, whereas the MetEx–Sil lower layer exhibited the lowest value. The bilayer construct demonstrated an intermediate tensile modulus between those of the individual layers, indicating robust interfacial integration without delamination. Similarly, the compression modulus followed an identical hierarchical trend: Ag–CS layer > bilayer > MetEx–Sil layer. These quantitative mechanical results align closely with the rheological profile (Figure 3I and 3J), collectively confirming that the bilayer dressing possesses adequate mechanical robustness for practical operation. The stiffness gradient combines a stiffer upper layer that resists external friction with a softer lower layer that ensures intimate wound bed contact, providing a mechanically rational design that will not break or fail during dressing application and daily activities.

#### 3.2.6. Swelling properties

Swelling curves revealed rapid liquid absorption during the initial immersion period for all groups, followed by gradual plateau formation, indicating significant water uptake and swelling before reaching equilibrium (Figure 3K). The overall swelling capacity ranked as: MetEx–Sil layer > Ag–CS/MetEx–Sil bilayer hydrogel > Ag–CS layer. Specifically, the lower layer exhibited the highest swelling ratio (~1350–1400% at 48 h), indicating high water absorption capacity and an open network structure. The upper layer exhibited the lowest swelling ratio (~700% at 48 h), suggesting a denser network that restricted further liquid penetration. The bilayer construct displayed an intermediate swelling ratio (~1,000% at 48 h), integrating the characteristics of the dense upper layer and porous lower layer. These results were consistent with microstructural observations, where the dense layer reduced overall liquid absorption rates while the porous layer enhanced liquid storage capacity.

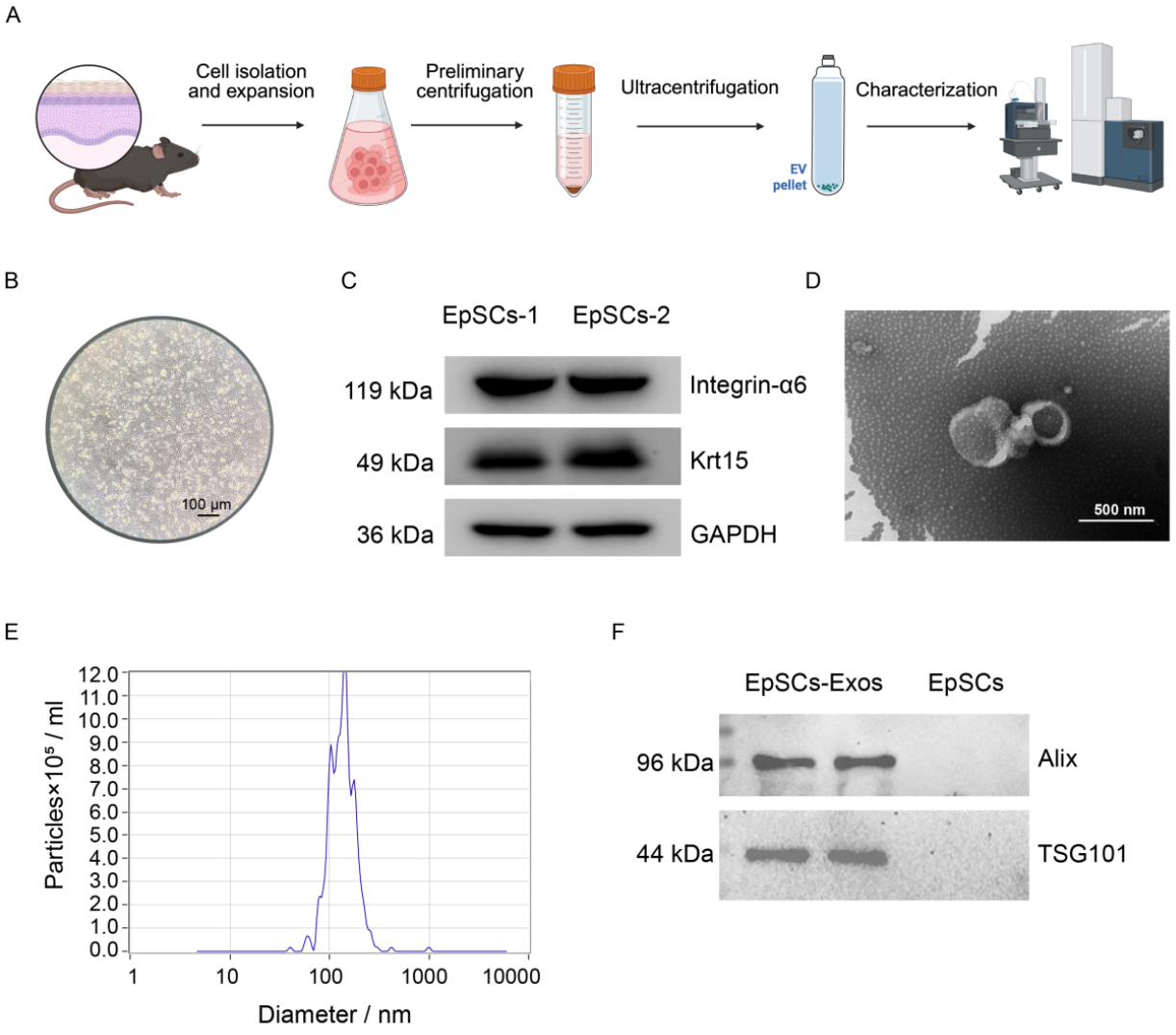


**Figure 2.** Isolation and characterization of EpSCs and EpSCs-Exos. (A) Schematic diagram illustrating the isolation of primary EpSCs from mouse skin and purification of exosomes via differential ultracentrifugation. Created in BioRender. Feng, Y. (2026) https://BioRender.com/ui4dbi9 (B) Representative bright-field image of primary EpSCs showing colony formation. Scale bar: 100 μm; magnification: 20×. (C) Western blot analysis of epithelial stem cell markers (integrin-α6 and Krt15) in two independent preparations. (D) Cryo-TEM image showing spherical vesicles with a characteristic phospholipid bilayer. Scale bar: 500 nm; magnification: 20,000×. (E) Nanoparticle tracking analysis size distribution of EpSCs-Exos (mean diameter: 133.2 nm; yield: 2.1 × $10^{11}$ particles/mL). (F) Western blot detection of exosomal markers (Alix and TSG101) in EpSCs-Exos compared to parental EpSCs.

### *3.2.7. Release profiles of $Ag^+$, metformin, and EpSCs-Exos from Ag–CS/MetEx–Sil hydrogel*

Release profiles of $Ag^+$, metformin, and EpSCs-Exos from the respective hydrogel layers were systematically evaluated over a 7-day period. As depicted in Figure 3L, the upper Ag–CS layer exhibited a rapid initial burst release of $Ag^+$, with 34.06 ± 0.83% of the total payload released within 1 day and 47.10 ± 1.12% cumulative release achieved by 2 days. This was followed by a sustained, gradual release phase, ultimately reaching 81.00 ± 3.25% cumulative release by 7 days. The lower MetEx–Sil layer exhibited similar kinetics for metformin and EpSCs-Exos. The metformin release profile (Figure 3M) displayed an initial rapid release with 37.01 ± 0.97% at 1 day, followed by a steady deceleration with 64.11 ± 2.12% cumulative release by 3 days, ultimately reaching 87.21 ± 4.43% by 7 days. This sustained metformin presence establishes a metabolically favorable and anti-inflammatory microenvironment within the deeper wound strata, which typically compromises exosomal integrity. Concurrently, EpSCs-Exos displayed a

rapid initial release with 47.15 ± 1.64% cumulative release within 1 day and 66.34 ± 1.22% by 2 days, followed by gradual sustained release, achieving 91.23 ± 4.91% by 7 days (Figure 3M). The 3D IF imaging confirmed that the exosomes were evenly distributed throughout the hydrogel and progressively diminished with prolonged immersion time (Figure 3N).

#### *3.2.8. Structural integrity of released exosomes*

To determine whether EpSCs-Exos retain their structural integrity after release from the MetEx–Sil layer, the release medium collected at day 3 was subjected to ultracentrifugation, and the recovered vesicles were examined by TEM. As shown in Figure S2, the released exosomes exhibited typical round or cup-shaped morphology with intact bilayer membranes, which were indistinguishable from freshly isolated exosomes. This confirms that the hydrogel environment and the release process do not disrupt the vesicular ultrastructure.

### 3.3. Biocompatibility of the Ag–CS/MetEx–Sil hydrogel

The biocompatibility of the Ag–CS/MetEx–Sil hydrogel system was systematically evaluated through cytocompatibility and hemocompatibility assessments.

Cell viability and adhesion were evaluated using calcein-AM/PI live/dead staining and CCK-8 assays. Live/dead staining indicated high cell viability and favorable adhesion in all experimental groups (Ag–CS, MetEx–Sil, and Ag–CS/MetEx–Sil) at days 1 and 3 (Figure 4A and 4B). Comparable cytocompatibility was confirmed in HUVECs, with live/dead staining showing minimal dead cells and robust green fluorescence across all material extract groups (Figure S3). Quantitative CCK-8 analysis further confirmed excellent cytocompatibility, with all groups maintaining high viability at day 5 (Figure 4C). Notably, the Ag–CS/MetEx–Sil group exhibited significantly higher viability than the Control group, thereby demonstrating its superior biocompatibility.

Hemocompatibility was evaluated using a direct contact hemolysis assay with fresh anticoagulated mouse blood (Figure 4D). Visual observation revealed that supernatants from all hydrogel groups remained colorless, in stark contrast to the red and transparent supernatant of the positive control, indicating minimal erythrocyte lysis. Quantitative analysis of absorbance at 450 nm demonstrated that hemolysis rates for all experimental groups were well below the 5% safety threshold for biomaterials.[28] These results confirmed that the Ag–CS/MetEx–Sil bilayer hydrogel exhibited excellent hemocompatibility.

### 3.4. Antibacterial activity of the Ag–CS layer

Skin infections are predominantly caused by *E. coli* and *S. aureus*.[29] The antibacterial efficacy of the Ag–CS layer was systematically evaluated against these two pathogens, using both live/dead staining assays and spread plate methods (Figure 5A). As illustrated in Figure 5B and 5F, fluorescence microscopy images revealed that the Control group exhibited predominantly green fluorescence, representing live bacteria with intact membranes, while the CS group exhibited a mixed population of green and red fluorescence, indicating partial bacterial membrane damage. The Ag–CS group showed intense red fluorescence, signifying extensive bacterial death (Figure 5D and 5H). Consistent with the live/dead staining assays, the Control group exhibited dense bacterial colonies on agar plates, indicating robust bacterial proliferation without any inhibitory effect, whereas the CS group demonstrated moderate antibacterial activity with visibly reduced but still considerable colony formation compared to the Control (Figure 5C and 5G). The Ag–CS composite displayed potent antibacterial capability, with almost complete inhibition of bacterial growth observed on the agar plates. Quantitative analysis of colony-forming units (CFUs) revealed that the antibacterial efficacy followed the order: Ag–CS > CS > Control, with the Ag–CS group showing significantly higher inhibition rates against both *S. aureus* and *E. coli* compared to the other groups ($p < 0.05$) (Figure 5E and 5I). These results collectively demonstrate that the Ag–CS layer effectively induces bacterial death and suggest a synergistic effect between CS and AgNPs in enhancing antibacterial performance.

### 3.5. Immunomodulation of the MetEx–Sil layer

To evaluate the immunomodulatory capacity of the MetEx–Sil layer within a diabetic inflammatory microenvironment, RAW264.7 macrophages were cultured in HGHF medium to mimic T2DM conditions *in vitro*, followed by exposure to material extracts (Control, Met–Sil, and MetEx–Sil) (Figure 6A).

Macrophage polarization was assessed by IF staining for CD86 (M1 marker) and Arg-1 (M2 marker).[30] IF staining demonstrated the Control group was characterized by prominent CD86-positive cells with sparse Arg-1 expression, whereas the MetEx–Sil group exhibited the inverse pattern, and the Met–Sil group displayed an intermediate immunophenotypic profile (Figure 6B). These observations were corroborated by quantitative analysis (Figure 6C).

To further quantify the phenotypic switch, flow cytometry was performed using antibodies against CD86 (M1-specific marker) and CD206 (M2-specific marker)

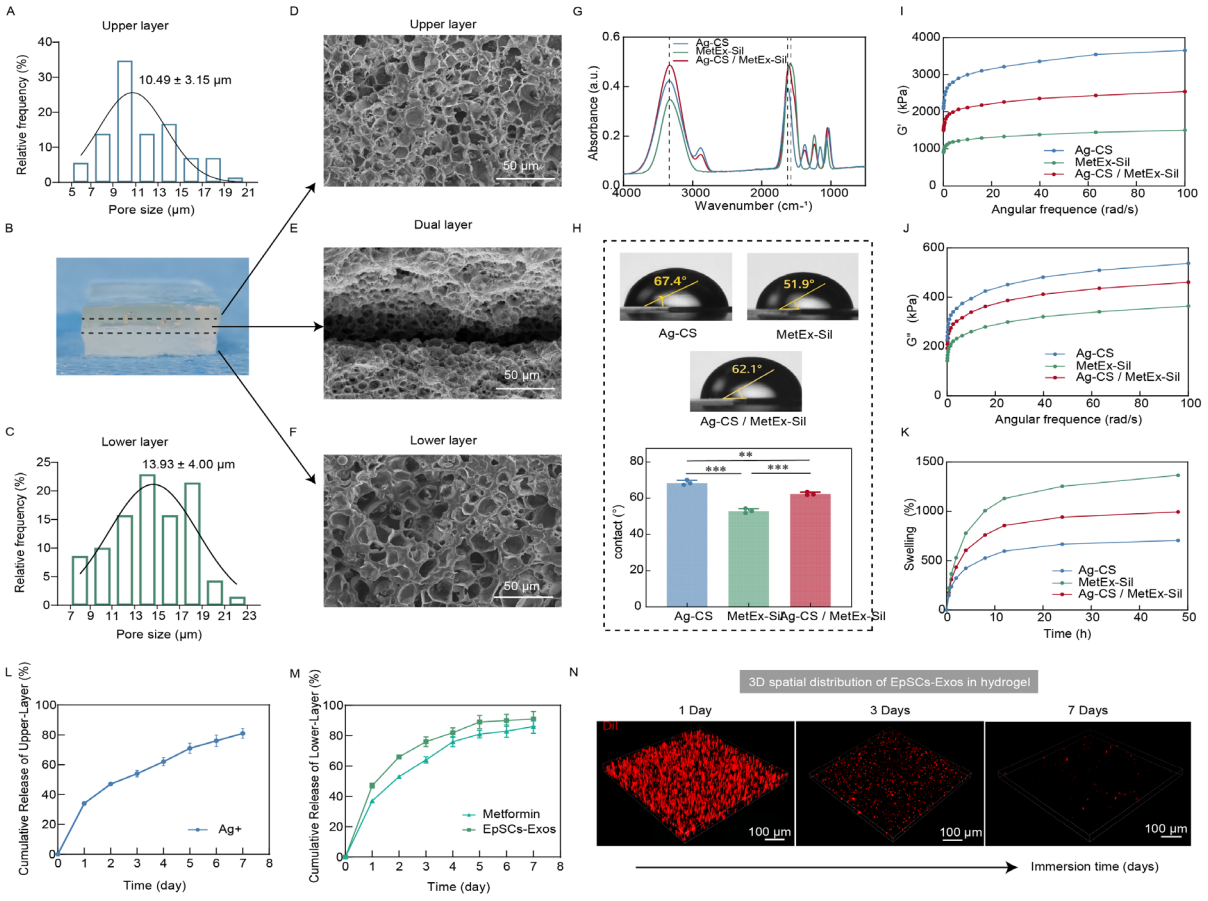


**Figure 3.** Characterization of the bilayer Ag–CS/MetEx–Sil hydrogel. (A, C) Pore size distribution histograms of the upper Ag–CS layer (A) and lower MetEx–Sil layer (C). (B) Photograph of the bilayer hydrogel showing distinct upper and lower layers. (D–F) Scanning electron microscopic images displaying the porous morphology of the upper layer (D; scale bars: 50 μm; magnification: 615×), the interfacial boundary between layers (E; scale bars: 50 μm; magnification: 400×), and the lower layer (F; scale bars: 50 μm; magnification: 615×). (G) Fourier transform infrared spectra confirming the chemical composition of individual layers and the bilayer construct. (H) Water contact angle measurements and quantitative analysis demonstrating surface wettability differences between layers ($n = 3$). (I, J) Frequency sweep rheological analysis showing storage modulus (G') (I) and loss modulus (G") (J) as a function of angular frequency. (K) Swelling kinetics of the hydrogels over 48 h. (L, M) *In vitro* $Ag^+$ release profile from the upper layer (L), and metformin and EpSCs-Exos from the lower layer (M) over 7 days. (N) 3D immunofluorescence imaging showing the spatial distribution and gradual release of EpSCs-Exos (red) from the hydrogel at days 1, 3, and 7. Scale bars: 100 μm; magnification: 20×. Data are presented as mean ± standard deviation.

on day 2 (Figure 6D and 6E). Consistent with IF staining results, the proportion of $CD206^+$ M2 macrophages was highest in the MetEx–Sil group (63.41 ± 4.35%), followed by Met–Sil (47.96 ± 6.75%) and Control (29.83 ± 4.52%). Conversely, the percentage of $CD86^+$ M1 macrophages decreased from 56.57 ± 6.24% (Control) to 30.12 ± 6.02% (Met–Sil) and further to 9.85 ± 2.65% (MetEx–Sil). These data suggest that MetEx–Sil most effectively suppressed pro-inflammatory M1 polarization while facilitating M2 conversion.

To assess the long-term durability of this immunomodulatory effect, flow cytometry was extended to day 7, a time point selected to match the sustained-release plateau of metformin and EpSCs-Exos (Figure 3M) and to cover the inflammatory-to-proliferative transition window critical for diabetic wound repair (Figure S4). Quantitative analysis confirmed that the MetEx–Sil group sustained a predominant M2 phenotype, with $CD206^+$ macrophages remaining significantly elevated and $CD86^+$ M1 macrophages persistently suppressed relative to the Control and Met–Sil groups. The Met–Sil group maintained an intermediate M2/M1 ratio, whereas the Control group retained a pro-inflammatory profile

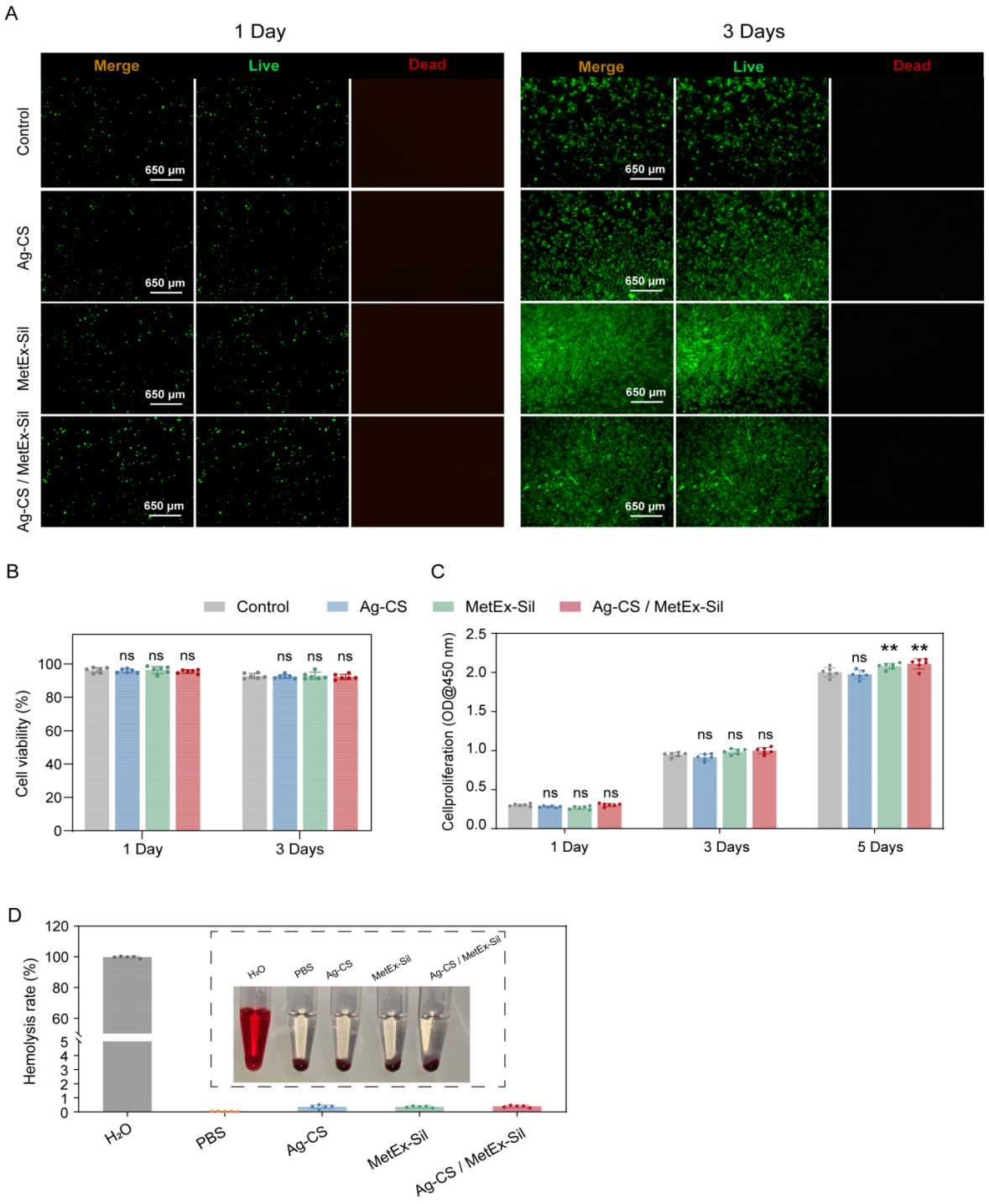


**Figure 4.** Biocompatibility evaluation of the Ag–CS/MetEx–Sil hydrogel. (A) Representative calcein-AM/PI live/dead staining images of human skin fibroblasts treated with extracts from different hydrogel groups (Control, Ag–CS, MetEx–Sil, and Ag–CS/MetEx–Sil) at days 1 and 3. Green fluorescence indicates live cells, while red fluorescence indicates dead cells. Scale bar: 650 μm; magnification: 20×. (B) Quantitative analysis of cell viability at days 1 and 3 based on live/dead staining. No statistically significant differences were observed among all groups ($p > 0.05$). (C) Cell proliferation measured by CCK-8 assay at days 1, 3, and 5, showing optical density (OD) values at 450 nm. (D) Hemocompatibility assessment via direct contact hemolysis assay. Left: Hemolysis rates calculated from absorbance at 450 nm; Right: Photographic images of supernatants after centrifugation ($H_2O$ as positive control, PBS as negative control). Statistical comparisons were conducted between the control group and each experimental group at the respective time point.

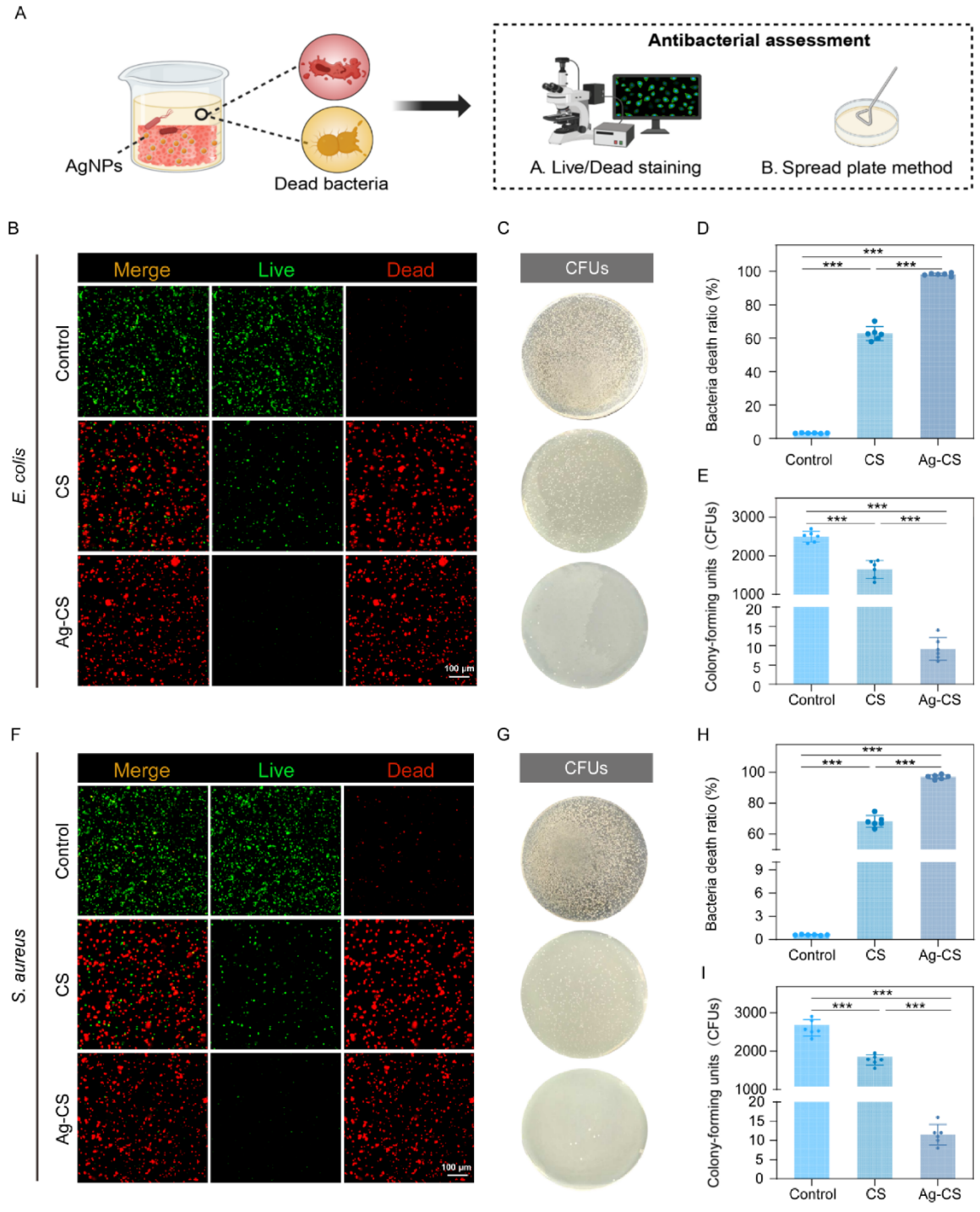


**Figure 5.** Antibacterial activity of the silver (Ag)–chitosan (CS) layer against *E. coli* and *S. aureus*. (A) Schematic diagram illustrating the antibacterial assessment methodology employing live/dead staining and spread plate methods. Created in BioRender. Feng, Y. (2026) https://BioRender.com/qhdh8m6 (B, F) Representative fluorescence microscopy images of live/dead staining for *E. coli* (B) and *S. aureus* (F). Green fluorescence indicates live bacteria with intact cell membranes, whereas red fluorescence indicates dead bacteria with compromised membranes. Scale bar: 100 μm; magnification: 80×. (C, G) Representative images of CFUs on agar plates for *E. coli* (C) and *S. aureus* (G). (D, H) Quantitative analysis of bacterial death ratio (%) for *E. coli* (D) and *S. aureus* (H). (E, I) Quantitative analysis of CFU counts for *E. coli* (E) and *S. aureus* (I). Data are presented as mean ± standard deviation. Statistical significance was determined by one-way ANOVA with Tukey's post-hoc test. Statistical significance is indicated by asterisks: $^{*}p < 0.05$, $^{**}p < 0.01$, $^{***}p < 0.001$.

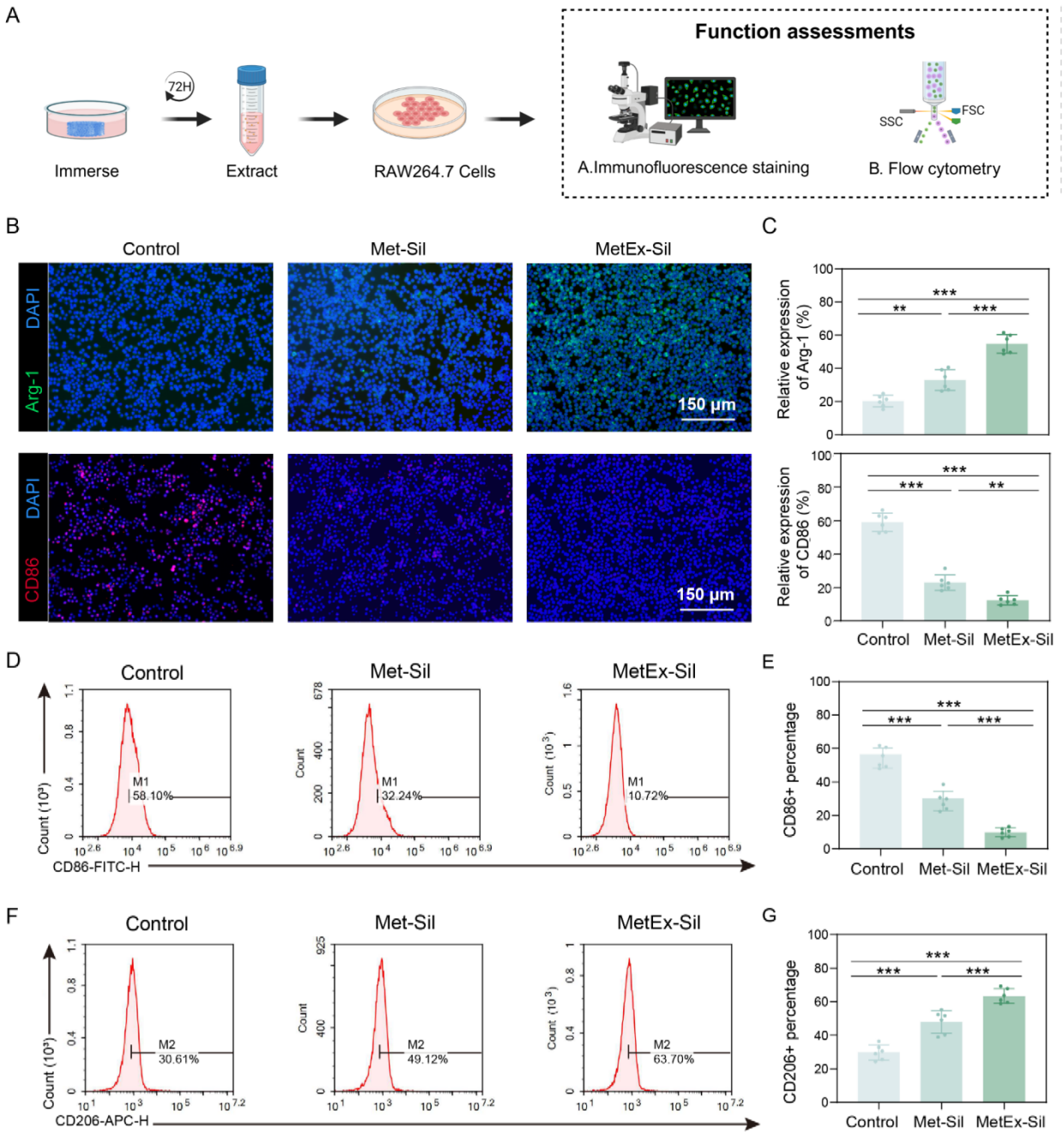


**Figure 6.** Immunomodulatory function of the MetEx–Sil layer on macrophage polarization in a diabetic microenvironment. (A) Schematic diagram illustrating the experimental workflow for evaluating immunomodulatory function. Created in BioRender. Feng, Y. (2026) https://BioRender.com/qhdh8m6 (B) Representative immunofluorescence images of RAW264.7 macrophages at day 2 post-treatment, stained for CD86 (red, M1 marker), Arg-1 (green, M2 marker), and DAPI (blue, nuclei). Scale bar: 150 μm; magnification: 20×. (C) Quantitative analysis of CD86 and Arg-1 relative expression (%) over time. (D, F) Representative flow cytometry histograms showing the expression of CD86 (M1 marker) (D) and CD206 (M2 marker) (F) at 2 days. (E, G) Percentages of $CD86^+$ (E) and $CD206^+$ (G) macrophage proportions. Data are presented as mean ± standard deviation. Statistical significance was determined by one-way ANOVA with Tukey's post-hoc test. Statistical significance is indicated by asterisks: $^*p < 0.05$, $^{**}p < 0.01$, $^{***}p < 0.001$.

throughout the 7-day observation period. These findings confirm that the M2-polarizing capacity of MetEx–Sil is not transient but durable over an extended duration, reinforcing its potential to maintain an anti-inflammatory microenvironment in chronic diabetic wounds.

### 3.6. Pro-angiogenic potential of the MetEx–Sil layer

To assess the pro-angiogenic properties of the MetEx–Sil layer, scratch assay and transwell assay were performed using HUVECs incubated with extracts from the Control, Met–Sil, and MetEx–Sil groups (Figure 7A).

As illustrated in Figure 7B and 7D, wound areas created by mechanical scratching exhibited differential closure rates among the three groups over 1 day and 2 days. At 1 day post-scratching, the scratch-gap closure rate in the MetEx–Sil group reached 79.61 ± 5.59%, which was significantly higher than that of the Met–Sil group (66.88 ± 5.93%) and the Control group (28.14 ± 5.27%). By 2 days, the MetEx–Sil group achieved near-complete wound closure (97.33 ± 3.64%), followed by the Met–Sil group (88.84 ± 4.45%), while the Control group showed only partial healing (51.47 ± 6.86%). The Met–Sil group demonstrated intermediate migratory activity, with scratch-gap closure rates significantly surpassing the Control at both 1 day and 2 days ($p < 0.05$), but remaining inferior to the MetEx–Sil group ($p < 0.05$), indicating metformin and EpSCs-Exos synergistically promote endothelial cell recruitment and migration.

Consistent with the scratch assay findings, the transwell assay revealed that the MetEx–Sil extract significantly enhanced the chemotactic migration of HUVECs toward the lower chamber (Figure 7C and 7E). Quantitative analysis of crystal violet-stained cells demonstrated that the number of migrated endothelial cells in the MetEx–Sil group (1104.67 ± 71.44 cells) was approximately 4.40-fold higher than that of the Control group (251.17 ± 37.69 cells) and 1.80-fold higher than the Met–Sil group (614.67 ± 66.10 cells). Collectively, these results demonstrated that the MetEx–Sil group exhibited the most potent pro-angiogenic activity, as evidenced by significantly accelerated wound closure and enhanced endothelial cell migration.

### 3.7. Transcriptomic analysis of underlying mechanisms

To investigate the regulatory mechanisms of MetEx–Sil layer under diabetic conditions, transcriptomic sequencing was performed on HUVECs cultured under HGHF conditions for 3 days (Figure 8A). Compared with the Control group, MetEx–Sil treatment induced significant transcriptomic reprogramming, identifying 126 DEGs, including 79 upregulated and 47 downregulated genes ($|\log_2 FC| > 1$, FDR < 0.05) (Figure 8B). Hierarchical clustering heatmap showed clear segregation of DEGs into functionally distinct clusters (Figure 8C). Notably, MetEx–Sil treatment upregulated gene sets associated with tissue repair and angiogenesis while downregulating inflammation-related genes, indicating a coordinated phenotypic shift from a pro-inflammatory state toward a pro-reparative endothelial state under HGHF conditions.

Gene Ontology enrichment analysis revealed that upregulated genes were significantly enriched in tissue repair and angiogenesis-related terms, including "tissue remodeling," "angiogenesis," and "blood vessel morphogenesis." In contrast, downregulated genes were predominantly associated with inflammatory regulation, such as "macrophage chemotaxis" and "acute-phase response," suggesting that MetEx–Sil effectively suppressed the pro-inflammatory phenotype induced by HGHF conditions (Figure 8D). GSEA further elucidated the molecular mechanisms underlying MetEx–Sil-mediated endothelial regulation (Figure 8E). The hypoxia-inducible factor 1 (HIF-1) and vascular endothelial growth factor (VEGF) signaling pathways showed significant positive enrichment, suggesting a transcriptomic association between MetEx–Sil treatment and these angiogenesis-related pathways. Conversely, the advanced glycation end products–receptor for advanced glycation end products (AGE–RAGE) signaling pathway in diabetic complications and the viral protein interaction with cytokine and cytokine receptor signaling pathway exhibited significant negative enrichment, suggesting potential alleviation of advanced glycation end product receptor-mediated oxidative stress and inflammatory cascades. Additionally, PPI network analysis identified two modules. As shown in Figure 8F, the pro-reparative module encompassed tissue repair- and angiogenesis-associated genes (e.g., *MMP1*, *TIMP1*, *JAG1*, *HMOX1*) that converged on central biological processes including tissue remodeling, collagen metabolic process, and angiogenesis. Correspondingly, Figure 8G illustrates an inflammation-enriched module comprising cytokine-related genes (e.g., *IL1B*, *SAA1*, *GDF15*, *EDN1*) functionally linked to cytokine activity, macrophage chemotaxis, and immune responses. Collectively, these findings demonstrate that MetEx–Sil drives a coordinated phenotypic shift from pro-inflammatory to pro-reparative states in diabetic endothelial cells via transcriptomic reprogramming.

### 3.8. *In vivo* therapeutic efficacy in a diabetic wound model

Building on the promising *in vitro* results, we evaluated the therapeutic potential of the Ag–CS/MetEx–Sil hydrogel

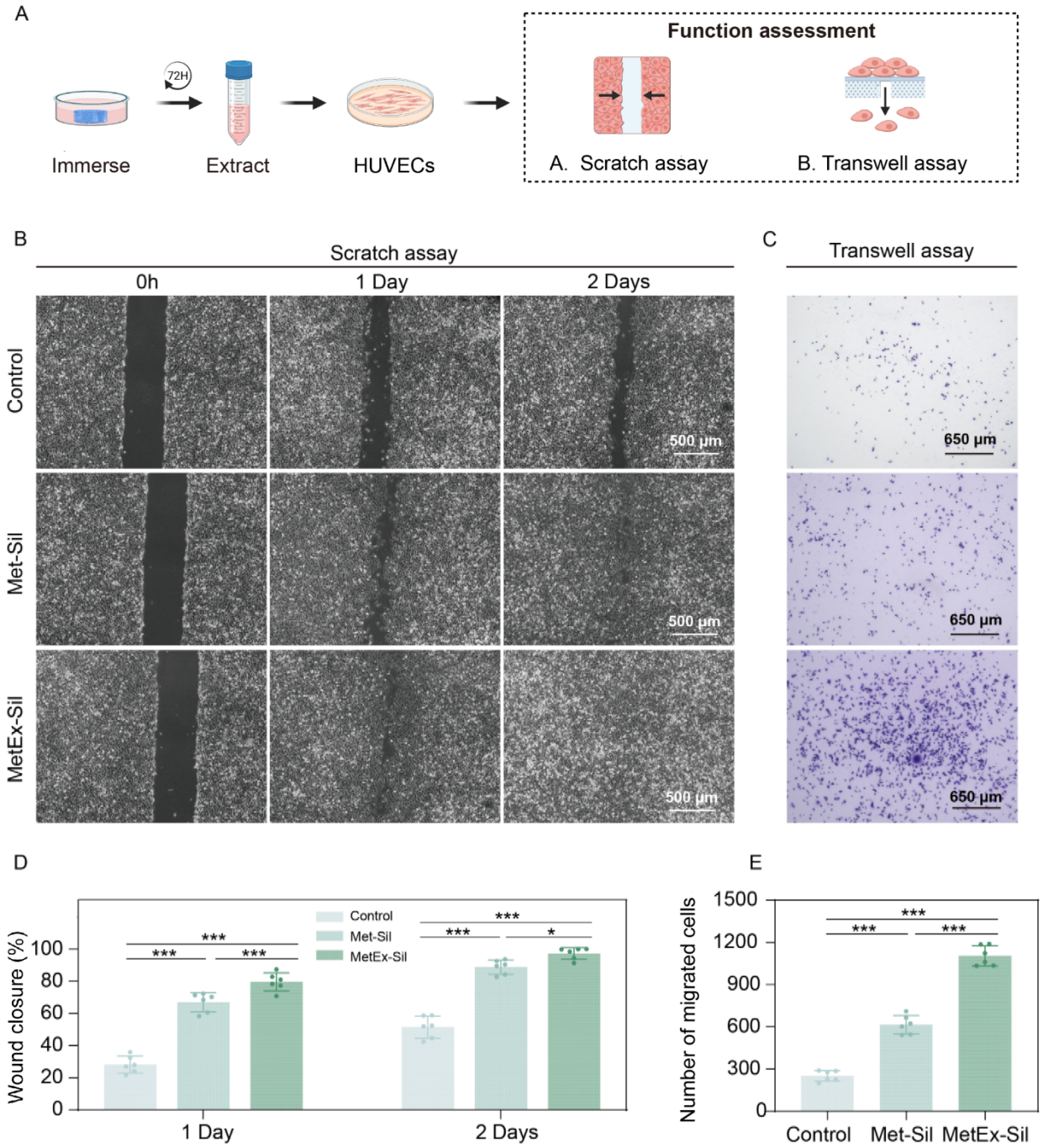


**Figure 7.** Pro-angiogenic potential of the MetEx–Sil layer in a diabetic microenvironment. (A) Schematic diagram illustrating the experimental workflow for evaluating pro-angiogenic capacity. Created in BioRender. Feng, Y. (2026) https://BioRender.com/qhdh8m6 (B) Representative bright-field images of the scratch assay showing wound closure at 0 h, 1 day, and 2 days. Scale bar: 500 μm; magnification: 20×. (C) Representative images of crystal violet-stained human umbilical vein endothelial cells (HUVECs) migrated through the transwell membrane. Scale bar: 650 μm; magnification: 20×. (D) Quantitative analysis of wound closure (%) at 1 and 2 days post-scratching. (E) Quantitative analysis of the number of migrated cells in the transwell assay. Data are presented as mean ± standard deviation. Statistical significance was determined by one-way ANOVA with Tukey's post-hoc test. Statistical significance is indicated by asterisks: *$p < 0.05$, **$p < 0.01$, ***$p < 0.001$.

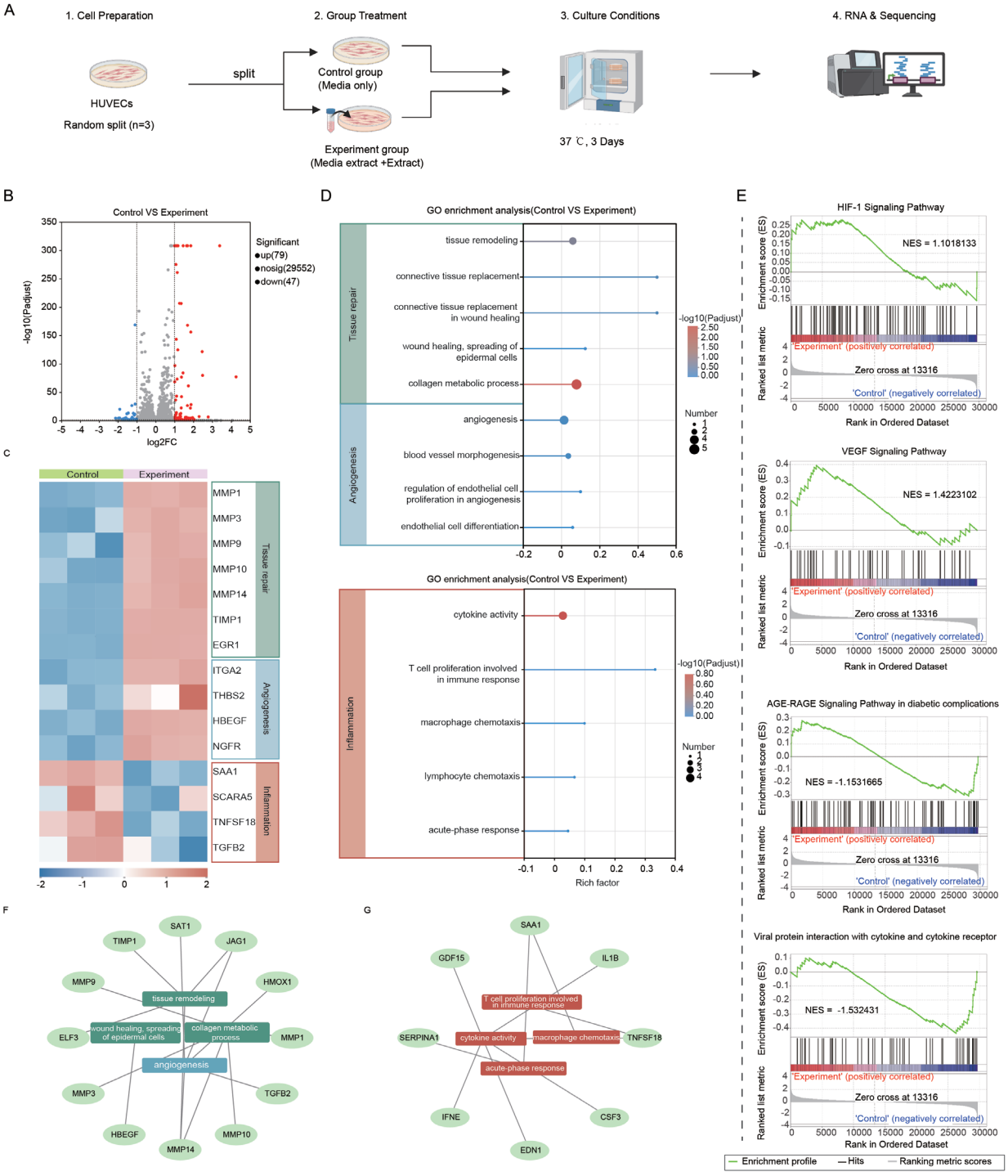


**Figure 8.** Transcriptomic analysis reveals molecular mechanisms of MetEx–Sil-mediated endothelial regulation in a diabetic microenvironment. (A) Schematic diagram illustrating RNA sequencing workflow in human umbilical vein endothelial cells (HUVECs). Created in BioRender. Feng, Y. (2026) https://BioRender.com/qhdh8m6 (B) Volcano plot showing differentially expressed genes (DEGs) between Control and Experiment groups ($|\log_2 FC| > 1$, false discovery rate < 0.05). (C) Hierarchical clustering heatmap of DEGs showing distinct expression patterns between groups. (D) Gene Ontology (GO) enrichment analysis of upregulated and downregulated genes. (E) Gene Set Enrichment Analysis revealing positive enrichment of hypoxia-inducible factor 1 (HIF-1) and vascular endothelial growth factor (VEGF) signaling pathways, and negative enrichment of AGE–RAGE signaling in diabetic complications, as well as cytokine-related pathways. (F, G) Protein–protein interaction network analysis identifying functional modules associated with (F) tissue repair/angiogenesis and (G) inflammatory responses.

dressing using a diabetic mouse model of infected full-thickness wounds on the dorsal skin. The experimental design is illustrated in Figure 9A. Wounds were treated with commercial gauze (Control), Ag–CS monolayer, MetEx–Sil monolayer, or Ag–CS/MetEx–Sil bilayer dressing at 1 day post-infection.

As shown in Figure 9B, wounds in all four groups gradually healed over 15 days. To quantitatively assess wound healing dynamics, residual wound areas were systematically measured at days 5, 10, and 15 post-treatment (Figure 9C). At day 15, the Control group exhibited limited healing with 8.93% ± 0.61% of the wound area remaining unclosed. The Ag–CS group demonstrated improved healing efficacy compared to Control, with 3.58% ± 0.39% residual wound area at day 15. The MetEx–Sil group showed accelerated wound closure, with 6.90% ± 0.54% of the wound remaining at day 15. Notably, the Ag–CS/MetEx–Sil combination group exhibited the most rapid re-epithelialization, achieving 3.15% ± 0.24% and 1.38% ± 0.11% remaining wound areas at days 10 and 15, respectively, indicating near-complete wound healing.

Systemic biosafety was further assessed by histopathological examination of major organs (heart, liver, spleen, lung, and kidney) at day 15. H & E staining revealed no discernible pathological abnormalities—including tissue necrosis, hemorrhage, or structural damage—across all treatment groups. Organs from the Ag–CS/MetEx–Sil group exhibited normal histoarchitecture comparable to that of the Control group, indicating that the bilayer dressing, and particularly the AgNP-embedded upper layer, did not elicit detectable systemic toxicity during the 15-day treatment period. Representative histological images are provided in Figure S5.

Microbial contamination represents a critical impediment to tissue regeneration and wound healing in diabetic models. To assess wound infection status, bacterial burden was quantified at day 5 using agar plate assays (Figure 9D). Consistent with the *in vitro* findings, both the Ag–CS and Ag–CS/MetEx–Sil treatment groups exhibited significant antibacterial activity, whereas the MetEx–Sil group demonstrated no discernible antibacterial effects.

Histological evaluation was subsequently performed at day 15 to further characterize tissue repair efficacy. H & E and Masson's trichrome staining were conducted to quantitatively assess granulation tissue thickness and collagen deposition. Quantitative analysis revealed that the Ag–CS/MetEx–Sil group displayed the greatest granulation tissue thickness (Figure 9E) and the most extensive collagen deposition among all treatment groups (Figure 9F), findings that were concordant between both staining modalities.

Inflammation, one of the hallmarks of chronic diabetic wounds, is closely related to macrophage polarization. We performed immunohistochemical staining for macrophage polarization markers at day 10. The Ag–CS/MetEx–Sil group demonstrated a favorable anti-inflammatory profile with markedly reduced CD86 and elevated CD163 expression compared to the Control group, suggesting that the bilayer dressing effectively promoted macrophage polarization toward the M2 phenotype (Figure 10A–10C). Revascularization sustains the hemodynamic support and metabolic substrate delivery requisite for creating a pro-regenerative niche in chronic diabetic wounds. Assessment of neovascularization via CD31 immunohistochemistry at day 15 revealed sparse microvascular density in Control wounds, while the Ag–CS/MetEx–Sil group exhibited significantly enhanced vascular density, consistent with the pro-angiogenic effect of loaded metformin and exosomes (Figure 10A and 10D).

## 4. Discussion

Impaired wound healing among diabetic patients poses a significant challenge in clinical practice. Chronic hyperglycemia leads to the accumulation of advanced glycation end-products in tissues, thereby triggering ongoing low-level inflammation, impairing microvascular oxygen and nutrient delivery, and compromising immune function.[31-33] Together, these factors create a wound environment that fundamentally differs from that of typical acute injuries and is characterized by prolonged healing times, increased risk of antibiotic-resistant bacterial infections, and potential progression to chronic, non-healing ulcers that may ultimately require amputation.[34,35] The superficial tissue requires immediate antibacterial protection and barrier function against external challenges, while deeper tissues need sustained bioactive signaling and an appropriate metabolic microenvironment to support gradual reconstruction. However, most existing monolayer scaffold designs are limited in their ability to simultaneously address these divergent requirements.

This study employed biomimetic principles based on the native architecture of skin to construct a composite scaffold system with distinct functional compartmentalization. As the body's largest organ, skin exhibits an epidermal-dermal stratified structure. The epidermis, primarily composed of keratinocytes arranged in a tightly packed stratified squamous epithelium, forms physical barriers through desmosomes and tight junctions, executing immune defense, moisture retention, UV protection, and sensory signal transduction functions.[36] The dermis, organized around a loose collagen and elastic

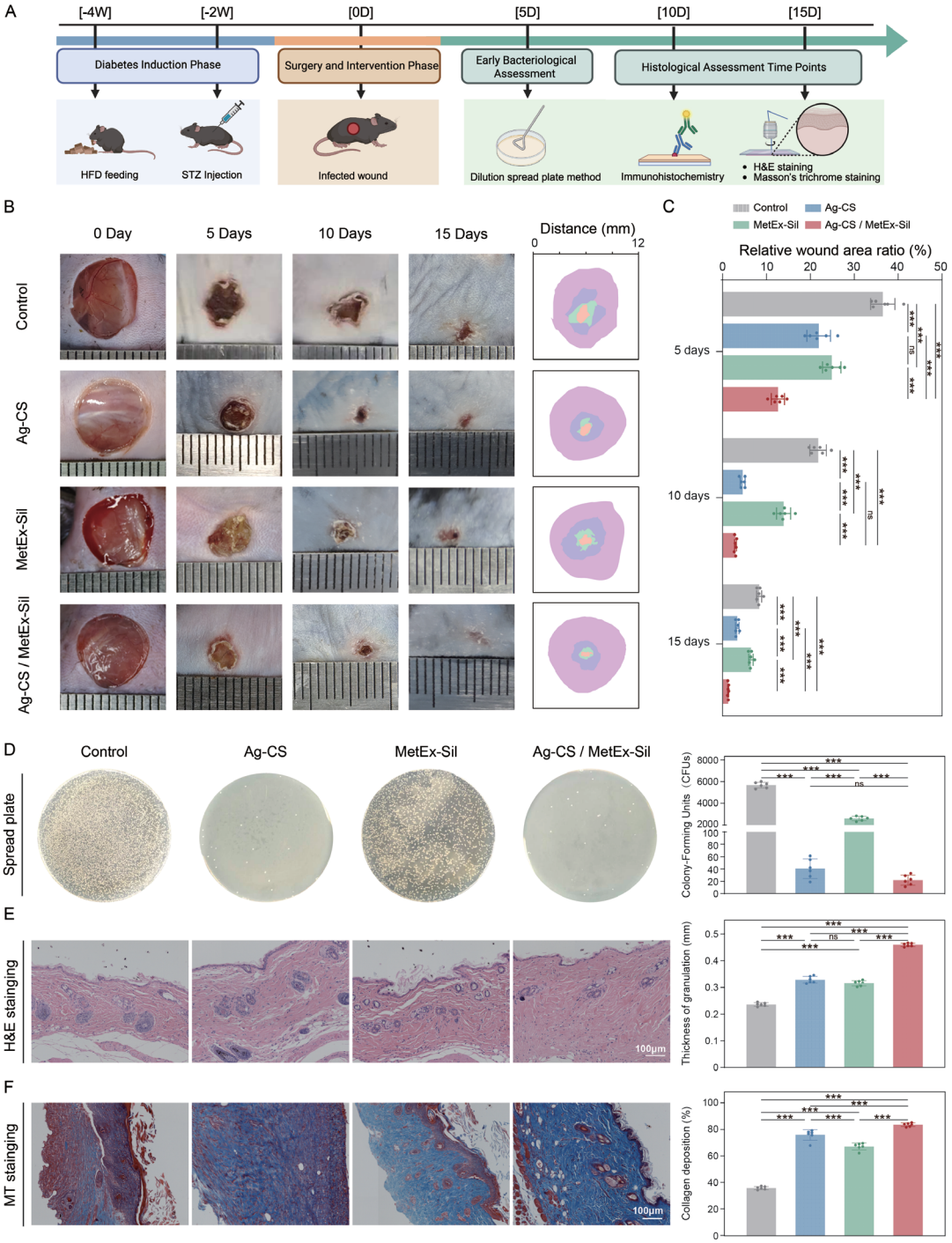


**Figure 9.** *In vivo* therapeutic efficacy of silver (Ag)–chitosan (CS)/MetEx–Sil hydrogel dressing in a diabetic mouse model of infected full-thickness wounds. (A) Schematic diagram illustrating the experimental timeline, including diabetes induction, surgery, and assessment time points. Created in BioRender. Feng, Y. (2026) https://BioRender.com/qhdh8m6 (B) Representative photographs of wound healing progression at 0, 5, 10, and 15 days post-treatment (left) with corresponding wound area schematic diagrams (right). (C) Quantitative analysis of remaining wound area (%) at days 5, 10, and 15. (D) Representative images of agar plate assays (left) and quantitative analysis of bacterial colony-forming units (CFUs) (right) at day 5. (E) Representative hematoxylin and eosin (H & E) staining images (left) and quantitative analysis of granulation tissue thickness (right) at day 15. Scale bar: 100 μm; magnification: 20×. (F) Representative Masson's trichrome (MT) staining images (left) and quantitative analysis of collagen deposition (%) (right) at day 15. Scale bar: 100 μm; magnification: 20×. Data are presented as mean ± standard deviation. Statistical significance was determined by one-way ANOVA with Tukey's post-hoc test. Statistical significance is indicated by asterisks: $^{*}p < 0.05$, $^{**}p < 0.01$, $^{***}p < 0.001$.
Abbreviations: HFD: High-fat diet; STZ: Streptozotocin.

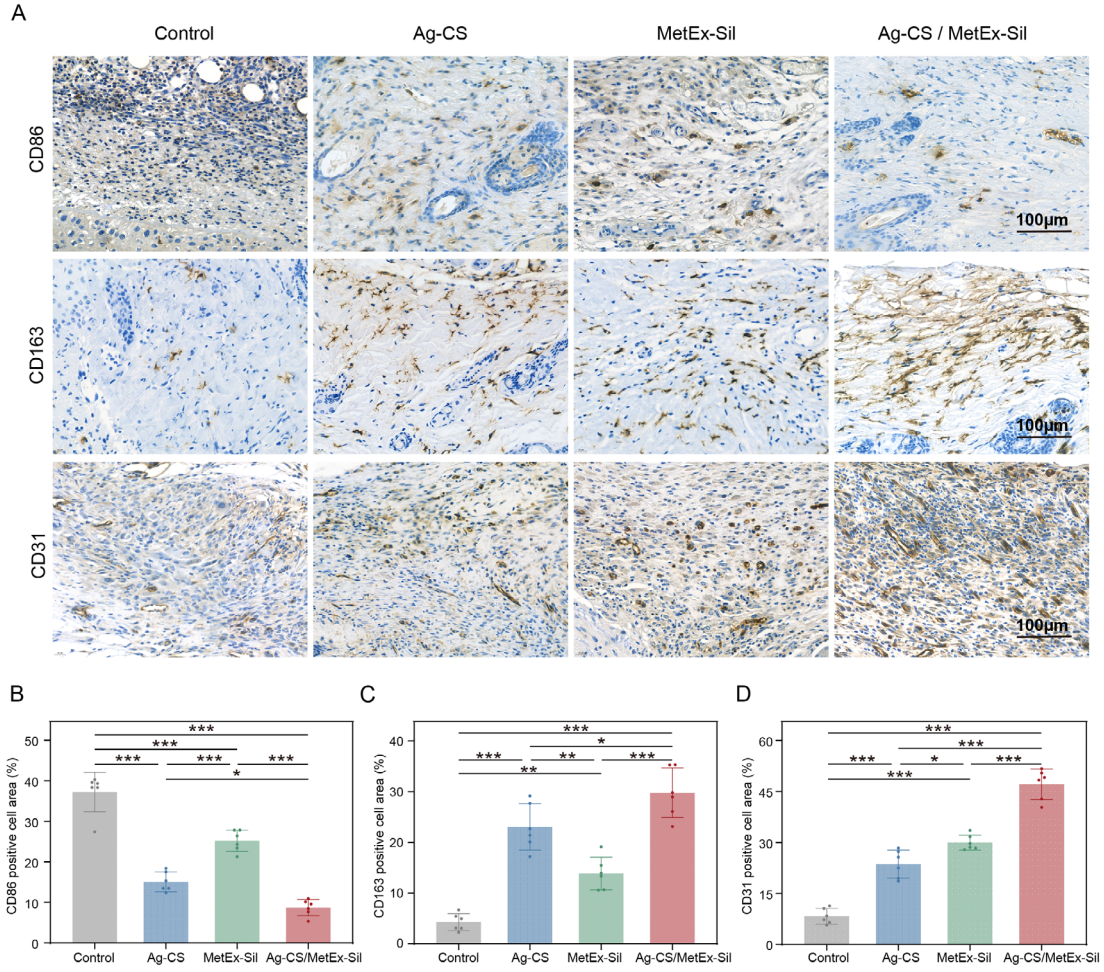


**Figure 10.** Immunohistochemical analysis of macrophage polarization and angiogenesis in diabetic wounds. (A) Representative immunohistochemical staining images for CD86 (M1 macrophage marker) and CD163 (M2 macrophage marker) at day 10, and CD31 (endothelial cell marker) at day 15. Scale bar: 100 μm; magnification: 40×. (B, C) Quantitative analysis of (B) CD86-positive and (C) CD163-positive cell area (%) at day 10. (D) Quantitative analysis of CD31-positive cell area (%) at day 15. Data are presented as mean ± standard deviation. Statistical significance was determined by one-way ANOVA with Tukey's post-hoc test. Statistical significance is indicated by asterisks: $^{*}p < 0.05$, $^{**}p < 0.01$, $^{***}p < 0.001$.

fiber network, accommodates vasculature, nerve endings, immune cells, and fibroblasts, fulfilling nutrient supply, metabolic exchange, sensory conduction, and tissue repair functions.[37] This functional division provided direct biomimetic templates for our material design.

The upper compartment utilized CS-based hydrogels embedded with AgNPs, with pore sizes of 10.49 ± 3.15 μm. Hydration-induced extension of CS molecular chains exposed protonatable amino groups, forming polycationic ammonium moieties that electrostatically compromised bacterial membrane integrity in both *S. aureus* and *E. coli*.[38] Simultaneously, AgNPs bind to thiol groups in bacterial proteins, disrupting electron transport in the respiratory chain. This synergistic approach addresses critical shortcomings of single-agent therapies. While pure CS requires extended contact times for membranolysis and AgNPs alone exhibit dose-dependent cytotoxicity risks, the composite establishes an active biochemical barrier against invading microorganisms. The resulting microenvironment suppresses bacterial colonization, thereby supporting undisturbed tissue regeneration. Although the Ag–CS layer contains AgNPs, the bilayer construct exhibited excellent cytocompatibility *in vitro*, with CCK-8 results showing higher OD values than the Control at day 5 (Figure 4C). This reflects the sub-toxic, sustained $Ag^{+}$ release from the CS matrix (47.1% and 81.0% cumulative release by days 2 and 7, respectively; Figure 3L), which keeps the effective concentration below

the cytotoxic threshold. Literature evidence confirms that nano-silver in biopolymer networks does not inherently abolish cell proliferation; at low sustained doses, it may induce a hormetic effect that enhances fibroblast proliferation.[39-41] Consequently, the hydrogel-buffered $Ag^+$ flux preserves the proliferative capacity of skin cells, allowing the pro-regenerative components in the lower layer to dominate the biological readout.

The lower compartment employed SilMA hydrogels co-encapsulating EpSCs-Exos and metformin. SF, already approved by the United States Food and Drug Administration for medical applications, exhibits excellent biocompatibility and tunable degradation characteristics. Methacrylate modification introduces photocrosslinkable sites, endowing SilMA with superior photopolymerization properties and 3D printability, enabling precise fabrication of customized scaffolds with designed porous architectures through digital light processing or extrusion-based bioprinting.[42] This co-encapsulation strategy establishes a unique "biological signal and metabolic modulation" synergistic delivery system. Exosomes, extracellular vesicles of 30–150 nm diameter, carry bioactive molecules including proteins, lipids, mRNA, and miRNA derived from parent cells, regulating target cell functions through paracrine mechanisms.[43] EpSC-Exos are enriched with pro-angiogenic miRNAs and growth factors, including VEGF, PDGF, and TGF-β, effectively activating endothelial cell proliferation, migration, and lumen formation while recruiting dermal fibroblasts and promoting their transformation toward synthetic phenotypes, enhancing collagen and matrix component secretion.[19-21] However, exosome monotherapy faces two limitations in diabetic wounds: (i) metabolic dysregulation and mitochondrial dysfunction in diabetic tissues impair cellular responsiveness to exosome-mediated signaling; (ii) preserving exosome bioactivity requires a metabolically favorable microenvironment that diabetic wounds typically lack. The incorporation of metformin addresses these challenges. Metformin, an oral hypoglycemic agent with over six decades of clinical use, has recently been shown to promote tissue repair independent of glycemic control. It activates adenosine monophosphate-activated protein kinase, inhibiting mechanistic target of rapamycin to induce autophagy and clear damaged mitochondria, thereby reducing reactive oxygen species and oxidative stress.[44,45] It also inhibits mitochondrial complex I, decreasing oxygen consumption and stabilizing HIF-1α to maintain pro-angiogenic signaling under hypoxia.[44,46] Critically, EpSCs-Exos and metformin exhibit synergistic functional coupling: exosomes drive cell recruitment and signal activation, while metformin provides sustained metabolic support and microenvironmental improvement, jointly ameliorating chronic inflammation in diabetic wounds.

In validation using an infected full-thickness skin defect model in diabetic mice, the Ag–CS/MetEx–Sil bilayer dressing achieved near-complete healing by day 15, significantly outperforming single-layer hydrogels. Bacteriological assessment on postoperative day 5 revealed significantly lower bacterial loads than those of the control group. Histological analysis at postoperative day 15 was characterized by maximal granulation tissue thickness and collagen deposition. Immunohistochemical results demonstrated significant upregulation of the M2 macrophage marker CD163, with concomitant reduction in the M1 marker CD86, suggesting that this dressing can transform the immune microenvironment of diabetic wounds from a pro-inflammatory to a pro-repair state. Furthermore, increased CD31-positive staining indicated enhanced neovascular network formation.

Nevertheless, this study has several limitations and suggests directions for future research. First, although CS and SF are clinically validated safe materials, the long-term tissue accumulation and potential cytotoxicity of AgNPs require more extended systematic observation. Furthermore, batch consistency control, activity preservation standards, and scalable GMP production workflows for exosomes represent critical bottlenecks for clinical translation, which necessitate the establishment of rigorous quality control systems. Second, while this study focused primarily on macroscopic outcome measures of wound healing, future investigations should employ single-cell RNA sequencing, spatial transcriptomics, and proteomics technologies to further dissect the regulatory mechanisms of the bilayer, particularly elucidating the molecular pathways through which metformin influences exosome uptake and signal transduction. Third, this study utilized diabetic mice without comorbidities as the animal model, without considering the complex conditions commonly associated with clinical diabetes, such as peripheral neuropathy and lower extremity arteriosclerosis. These factors may affect the actual efficacy and necessitate further validation of its performance under such conditions. Fourth, while *in vivo* efficacy was confirmed, the mechanistic analysis remained limited to endpoint histopathology and immunohistochemistry at fixed time points. Dynamic *in vivo* tracking of immune cell behavior, neovascularization, and exosome fate was not conducted and represents a direction for future investigation. With advances in 3D bioprinting, microfluidic technologies, and artificial intelligence-assisted design, future prospects include digital modeling and precise scaffold customization

based on patient-specific wound morphologies and pathological characteristics, which will drive diabetic wound treatment toward an integrated "diagnosis-material-repair" precision medicine paradigm.

## 5. Conclusion

This study presents a biomimetic bilayer hydrogel that translates skin stratification into a spatiotemporally programmed drug delivery platform. By segregating rapid surface antibacterial release from sustained deep-layer pro-regenerative delivery, the system effectively reconciled the competing demands of infection control and tissue regeneration. *In vivo* evaluation demonstrated significant enhancement in wound healing kinetics, including bacterial clearance, accelerated re-epithelialization, and improved angiogenesis in a diabetic wound model. These findings underscore the therapeutic potential of bioinspired architectural design in addressing the complex pathophysiology of chronic wounds. Future integration with 3D bioprinting technology may enable patient-specific customization, advancing precision management of diabetic ulcers.

## Acknowledgments

We thank Prof. Yafei Feng for his assistance with the graphical illustrations in this manuscript.

## Funding

This work was supported by the National Natural Science Foundation of China (82472487).

## Conflict of interest

The authors declare that they have no competing interests.

## Author contributions

*Conceptualization:* Shanshan Fu, Jing Wang, Wei Lei
*Formal analysis:* Haiyang Qiu, Qinghua Guo
*Investigation:* Wei Cao, Danxi Li, Qilong Yang
*Methodology:* Wei Cao, Danxi Li, Qilong Yang
*Writing–original draft:* Wei Cao
*Writing–review & editing:* Danxi Li, Qilong Yang, Shanshan Fu, Jing Wang

## Ethics approval and consent to participate

The animal experiments were approved by the Institutional Animal Care and Use Committee of the Air Force Medical University (Approval No. IACUC-20240561).

## Consent for publication

Not applicable.

## Availability of data

Data are available from the corresponding author upon reasonable request.

## References

1. Shah J, McKnight G, Hargest R. Physiology of the skin. *Surgery*. 2024;42(11):788-792.

   doi: 10.1016/j.mpsur.2024.09.008

2. Yadav JP, Singh AK, Grishina M, *et al.* Insights into the mechanisms of diabetic wounds: pathophysiology, molecular targets, and treatment strategies through conventional and alternative therapies. *Inflammopharmacology*. 2024;32(1):149-228.

   doi: 10.1007/s10787-023-01407-6

3. Lin H, Wang Z, Li P, *et al.* Intelligent-responsive hydrogel synergistically mediates immune remodel-antibacterial-angiogenesis cascade for diabetic foot ulcer repair. *Bioact Mater*. 2026;62:508-525.

   doi: 10.1016/j.bioactmat.2026.03.034

4. McDermott K, Fang M, Boulton AJM, Selvin E, Hicks CW. Etiology, Epidemiology, and Disparities in the Burden of Diabetic Foot Ulcers. *Diabetes Care*. 2023;46(1):209-221.

   doi: 10.2337/dci22-0043

5. Armstrong DG, Tan T-W, Boulton AJM, Bus SA. Diabetic foot ulcers: a review. *JAMA*. 2023;330(1):62–75.

   doi: 10.1001/jama.2023.10578

6. Han D, Ma C, Wang Y, *et al.* Application of one-step transplantation of acellular allogeneic dermis combined with autologous split-thickness skin graft in repairing deep burn wounds in functional areas of children. *Burns*. 2026;52(5):107914.

   doi: 10.1016/j.burns.2026.107914

7. Fu M, Huang Z, Li J, *et al.* Approaching Scarless Wound Healing: From Passive Anti-Fibrotic to Proactive and Programmable Pro-Regenerative Strategies. *Adv Sci*. 2026;13(18):e21824.

   doi: 10.1002/advs.202521824

8. Boyce ST, Simpson PS, Rieman MT, *et al.* Randomized, Paired-Site Comparison of Autologous Engineered Skin Substitutes and Split-Thickness Skin Graft for Closure of Extensive, Full-Thickness Burns. *J Burn Care Res*. 2017;38(2):61-70.

   doi: 10.1097/BCR.0000000000000401

9. Qin X, Wang Y, Feng Y, *et al.* Potentiating Chemo-Immunotherapy via a Programmable Nanocapsule-Hydrogel Platform for Sequential Tumor Microenvironment Remodeling. *Adv Mater*. 2026;38(14):e22016.

   doi: 10.1002/adma.202522016

10. Zheng B, Lu Z, Wang S, *et al.* Computational design of superstable proteins through maximized hydrogen bonding. *Nat Chem*. 2026;18(2):364-373.

doi: 10.1038/s41557-025-01998-3

11. Zhuo H, Liu Q, Dong X, Zheng H, Hong L, Zhai W. Superior Impact-Resistant Composite Hydrogels Through an Ionic Coupling Strategy. *Adv Mater*. 2026;38(26).

doi: 10.1002/adma.73010

12. Zhao X, Jiang X, Liang B, *et al.* A Bio-Orthogonal Engineered Chitosan Platform for Enhanced Mesenchymal Stem Cells Delivery and Function in Peripheral Nerve Repair. *Adv Mater*. 2026;38(13):e23237.

doi: 10.1002/adma.202523237

13. Elajaili H, Lyttle BD, Lewis CV, *et al.* Increased ROS and Persistent Pro-Inflammatory Responses in a Diabetic Wound Healing Model (db/db): Implications for Delayed Wound Healing. *Int J Mol Sci*. 2025;26(10):4884. 2025;26(10):4884.

doi: 10.3390/ijms26104884

14. Lin S, Wang Q, Huang X, *et al.* Wounds under diabetic milieu: The role of immune cellar components and signaling pathways. *Biomed Pharm*. 2023;157:114052.

doi: 10.1016/j.biopha.2022.114052

15. Murali N, Aastha, Das SB, *et al.* Magnetoelectrically Enhanced Molecular Recognition on Plasmonic Surfaces. *Small*. 2026;22(27).

doi: 10.1002/smll.202510657

16. Liu X, Meng L, Deng W, *et al.* Photo-induced in-situ synthesized nanocellulose-based SERS substrate integrated with molecularly imprinted polymer for selective detection of pesticide residues. *Carbohydr Polym*. 2026;380:125050.

doi: 10.1016/j.carbpol.2026.125050

17. Akter M, Sikder MT, Rahman MM, *et al.* A systematic review on silver nanoparticles-induced cytotoxicity: Physicochemical properties and perspectives. *J Adv Res*. 2017;9:1-16.

doi: 10.1016/j.jare.2017.10.008

18. Wong TY, Wang Y, Kwan KKL, *et al.* Exploring the Potentials of Silver Nanoparticles in Overcoming Cisplatin Resistance in Lung Adenocarcinoma: Insights from Proteomic and Xenograft Mice Studies. *ACS Nano*. 2025;19(39):34708-34723.

doi: 10.1021/acsnano.5c09056

19. Shin KO, Lee JH, Chae S, *et al.* Small EVs From Adipose-Derived MSCs Modulate Epidermal Barrier and Inflammation Via Sphingosine-1-Phosphate Signaling Pathway. *J Extracell Vesicles*. 2025;14(7):e70121.

doi: 10.1002/jev2.70121

20. Zhao S, Kong H, Qi D, *et al.* Epidermal stem cell derived exosomes-induced dedifferentiation of myofibroblasts inhibits scarring via the miR-203a-3p/PIK3CA axis. *J Nanobiotechnol*. 2025;23(1):56.

doi: 10.1186/s12951-025-03157-9

21. Duan M, Zhang Y, Zhang H, Meng Y, Qian M, Zhang G. Epidermal stem cell-derived exosomes promote skin regeneration by downregulating transforming growth factor-β1 in wound healing. *Stem Cell Res Ther*. 2020;11(1):452.

doi: 10.1186/s13287-020-01971-6

22. Tan F, Li X, Wang Z, Li J, Shahzad K, Zheng J. Clinical applications of stem cell-derived exosomes. *Signal Transduct Target Ther*. 2024;9(1):17.

doi: 10.1038/s41392-023-01704-0

23. Zhou C, Zhang B, Yang Y, *et al.* Stem cell-derived exosomes: emerging therapeutic opportunities for wound healing. Stem *Cell Res Ther*. 2023;14(1):107.

doi: 10.1186/s13287-023-03345-0

24. Luong JHT. Chitosan nanocrystals as next-generation antimicrobials: Mechanistic insights, antibiotic synergy, and biomedical potential. *Biotechnol Adv*. 2026;90:108879.

doi: 10.1016/j.biotechadv.2026.108879

25. Kim SH, Hong H, Ajiteru O, *et al.* 3D bioprinted silk fibroin hydrogels for tissue engineering. *Nat Protoc*. 2021;16(12):5484-5532.

doi: 10.1038/s41596-021-00622-1

26. Zheng Z, Yang X, Liu X, *et al.* A multifunctional hyaluronic acid hydrogel with pH-responsive metformin release for accelerated healing of diabetic infected wounds. *Mater Today Bio*. 2025;36:102755.

doi: 10.1016/j.mtbio.2025.102755

27. Xue Y, Fan L, Liu H, *et al.* Photo-crosslinkable hydrogel with programmable dual time-phase drug release for accelerated healing of infected diabetic wounds. *J Adv Res*. 2025.

doi: 10.1016/j.jare.2025.11.015

28. Nascimbene A, Bark D, Smadja DM. Hemocompatibility and biophysical interface of left ventricular assist devices and total artificial hearts. *Blood*. 2024;143(8):661-672.

doi: 10.1182/blood.2022018096

29. Licini C, Morroni G, Lucarini G, *et al.* ER-mitochondria association negatively affects wound healing by regulating NLRP3 activation. *Cell Death Dis*. 2024;15(6):407.

doi: 10.1038/s41419-024-06765-9

30. Qin H, Xie Z, Wang Y, *et al.* A hierarchical dexamethasone-loaded zeolitic imidazolate framework-8 hybrid coating on biodegradable ZnCu alloys for coordinated immuno-angiogenic-osteogenic and antibacterial regulation in inflammation-impaired fracture healing. *Biomaterials*.

2026;328:123875.

doi: 10.1016/j.biomaterials.2025.123875

31. Shen Z, Du L, Fang X, *et al.* Nanozyme Cryogel Accelerates Diabetic Wound Healing by Targeting Biofilms and Inflammations of the Wound Bed. *ACS Nano*. 2025;19(39):35081-35101.

doi: 10.1021/acsnano.5c12513

32. Adeshara K, Di Marco E, Bordino M, *et al.* Altered oxidant and antioxidant levels are associated with vascular stiffness and diabetic kidney disease in type 1 diabetes after exposure to acute and chronic hyperglycemia. *Cardiovasc Diabetol*. 2024;23(1):350.

doi: 10.1186/s12933-024-02427-4

33. Kang HJ, Kumar S, D'Elia A, *et al.* Self-assembled elastin-like polypeptide fusion protein coacervates as competitive inhibitors of advanced glycation end-products enhance diabetic wound healing. *J Control Release*. 2021;333:176-187.

doi: 10.1016/j.jconrel.2021.03.032

34. Zhang YQ, Nie R, Feng ZY, *et al.* Activating the cellular scavenger: A bioactive hydrogel promotes diabetic wounds via plant exosome-like nanovesicles enhanced macrophage efferocytosis. *Bioact Mater*. 2026;62:669-685.

doi: 10.1016/j.bioactmat.2026.03.039

35. Shi Y, Guo S, Tian J, *et al.* Biomaterials-mediated sequential drug delivery: Emerging trends for wound healing. *Asian J Pharm Sci*. 2025;20(6):101088.

doi: 10.1016/j.ajps.2025.101088

36. Agramunt J, Kang Y, Rinkevich Y. Spatiotemporal dynamics of mammalian wound healing. *Cell Discov*. 2026;12(1):4.

doi: 10.1038/s41421-025-00865-2

37. Thau H, Gerjol BP, Hahn K, *et al.* Senescence as a molecular target in skin aging and disease. *Ageing Res Rev*. 2025;105:102686.

doi: 10.1016/j.arr.2025.102686

38. Wang L, Pang Y, Xin M, Li M, Shi L, Mao Y. Effect of the structure of chitosan quaternary ammonium salts with different spacer groups on antibacterial and antibiofilm activities. *Int J Biol Macromol*. 2024;276(Pt 1):133777.

doi: 10.1016/j.ijbiomac.2024.133777

39. Huang WC, Ying R, Wang W, *et al.* A macroporous hydrogel dressing with enhanced antibacterial and anti-inflammatory capabilities for accelerated wound healing. *Adv Funct Mater*. 2020;30(21).

doi: 10.1002/adfm.202000644

40. Li Y, Yong D, Shen J, Bian R, Wang Y. Silver nanoparticle-loaded konjac glucomannan/silk fibroin composite hydrogels for enhanced wound healing. *Int J Biol Macromol*. 2025;300:140199.

doi: 10.1016/j.ijbiomac.2025.140199

41. Zhu J, Zeng Q, Liu Y, *et al.* Smart nanosilver strikes twice: precision bacteria killing meets autophagy-boosted healing for infected wounds. *Adv Funct Mater*. 2025;35(48).

doi: 10.1002/adfm.202507797

42. He X, Wang R, Zhou F, Liu H. Recent advances in photo-crosslinkable methacrylated silk (Sil-MA)-based scaffolds for regenerative medicine: A review. *Int J Biol Macromol*. 2024;256(Pt 1):128031.

doi: 10.1016/j.ijbiomac.2023.128031

43. Jun I, Ahn JY, Ahn G, *et al.* Exosome immobilization of 3D-printed polycaprolactone scaffolds for bone tissue engineering. *Int J Bioprinting*. 2026;12(2):026030021.

doi: 10.36922/IJB026030021

44. Kulkarni AS, Gubbi S, Barzilai N. Benefits of Metformin in Attenuating the Hallmarks of Aging. *Cell Metab*. 2020;32(1):15-30.

doi: 10.1016/j.cmet.2020.04.001

45. Packer M. Autophagy-dependent and -independent modulation of oxidative and organellar stress in the diabetic heart by glucose-lowering drugs. *Cardiovasc Diabetol*. 2020;19(1):62.

doi: 10.1186/s12933-020-01041-4

46. Wang YR, Zhang XX, Chen XX, *et al.* Enhancement of Bone Repair in Diabetic Rats with Metformin-Modified Silicified Collagen Scaffolds. *Adv Healthc Mater*. 2025;14(3):e2401430.

doi: 10.1002/adhm.202401430